Journal of Materials Chemistry A

REVIEW

View Article Online
View Journal | View Issue

Cite this: J. Mater. Chem. A, 2023, 11, 7358

Recent progress in block copolymer soft-template-assisted synthesis of versatile mesoporous materials for energy storage systems

Keon-Woo Kim,[ab] Bomi Park,[ab] Jun Kim,[ab] Changshin Jo*[bc] and Jin Kon Kim *[ab]

Received 1st December 2022
Accepted 5th March 2023

DOI: 10.1039/d2ta09353g

rsc.li/materials-a

Soft-templating methods, which utilize the block copolymer (BCP)-derived self-assembly with inorganic precursors, have been extensively applied to synthesize a wide range of mesoporous materials. Compared with other synthetic approaches including template-free and hard templating methods, the soft-templating method offers significant advantages for customizing various compositions, particle morphologies, and pore sizes/structures of mesoporous materials. During the last decade, various soft templating approaches have been developed to synthesize functional mesoporous materials for a variety of applications. In this review, we outline recent developments in synthetic approaches for mesoporous materials and their potential applications, particularly in energy storage systems (ESSs) such as batteries and supercapacitors. In addition, this review provides general information about soft-templating methods which can be applied to the tailored synthesis for the specific requirements of various applications.

1. Introduction

To provide a stable supply that meets the massive energy requirement of modern society, effective energy storage systems (ESSs) should be developed.[1–13] Energy storage devices broadly consist of electrolytes, active materials, and current collectors.[14,15] In general, energy storage is achieved through the redox reaction between the electrolyte and active materials.[16–25] Therefore, increasing the interfacial contact area has been considered as an effective strategy to enhance device performance.[3,26–36] This consideration has influenced many research groups to focus on controlling the physical architecture of active materials.[27–30]

Porous materials have several advantages owing to the presence of pores and voids within their structure. First, the high surface area of porous materials provides numerous active sites that can interact with electrolytes in oxidation/reduction reactions. Second, the porous structure significantly reduces the diffusion distance for adsorption/desorption of ions, enabling stable charging/discharging under fast operating conditions. In addition, the characteristics of porous materials

[a]National Creative Research Initiative Center for Hybrid Nano Materials By High-Level Architectural Design of Block Copolymer, Republic of Korea
[b]Department of Chemical Engineering, Pohang University of Science and Technology (POSTECH), Pohang, Gyungbuk 790-784, Republic of Korea. E-mail: jochangsihn@postech.ac.kr; jkkim@postech.ac.kr
[c]Graduate Institute of Ferrous & Energy Materials Technology (GIFT), Pohang University of Science and Technology (POSTECH), Republic of Korea

Keon-Woo Kim received a B.S. degree in polymer science & engineering from Yeungnam University in Korea (2017). Currently he is a PhD candidate in chemical engineering at POSTECH, Republic of Korea, under the supervision of Prof. Jin Kon Kim since 2017. His research interests include synthesis of nanomaterials and their application to printing technologies and electrochemical devices.

Bomi Park received a B.S. degree in chemistry from POSTECH (2022). Currently she is a M.S. candidate in chemical engineering at POSTECH, Republic of Korea, under the supervision of Prof. Jin Kon Kim since 2022. Her research interests include synthesis of mesoporous materials by using block copolymers and their application in energy storage systems.

depend on the type of porous structure. For example, porous materials with bicontinuous structures allow efficient mass and ion transport to the interior of the materials, maximizing active sites. In contrast, porous materials with discrete pores are ineffective in mass and ion transport due to the low connectivity of pores.[33,37–43]

Porous materials are divided into three categories according to pore size, namely, macropores (>50 nm), mesopores (2–50 nm), and micropores (<2 nm),[44–46] and show several (dis) advantages depending on the pore size. For instance, despite their extremely high surface areas, microporous materials are not suitable for efficient mass transport owing to their small pore size.[15,47–49] Meanwhile, macroporous materials facilitate mass transport owing to their large pore sizes, but their surface area is not sufficient to achieve high energy storage performance.[50–52] Mesoporous materials complement the features of the other two types. Because of their high surface area and large pore size, they have been widely used for catalysts,[53,54] energy storage systems,[55–59] and sensors.[60,61] In particular, the high surface area allows the effective loading of host materials, which increases the energy storage capacity and allows effective charge transfer between the mesoporous framework and host materials. In addition, the interconnected large pores provide structural stability by relieving the volume expansion and strain applied to the material during repeated charge/discharge cycles.[62–68]

Several methods, such as hard and soft templating, have been developed to synthesize mesoporous materials. Hard templating typically uses mesoporous silica,[48,62] carbon,[48] and colloidal crystals[69] as sacrificial templates. Benefiting from the thermal stability of the hard template, this method can produce various mesoporous materials with high crystallinities. However, this method requires the time-consuming process of preparation of a sacrificial template. In addition, the use of corrosive solvents for template removal restricts composition versatility and synthesis flexibility because they often dissolve several metal oxides and substrates.[5,70–72] On the other hand, the soft-templating method can effectively synthesize mesoporous materials because it mainly uses organic materials such as small molecular surfactants or block copolymers (BCPs) as both structure directing agents (SDAs) and templates, which are easy to control their molecular weight and chemical composition and easy to remove. For example, precursors of a target material are filled in pre-assembled BCPs followed by induction of the reaction. After removing the BCPs through solvent extraction, mesoporous materials are obtained. Instead of the above sequential synthetic approach, direct co-assembly of the precursors with SDAs is mainly used to form a mesostructured composite, which does not require a pre-assembly process of BCPs. The obtained mesostructured composites are finally

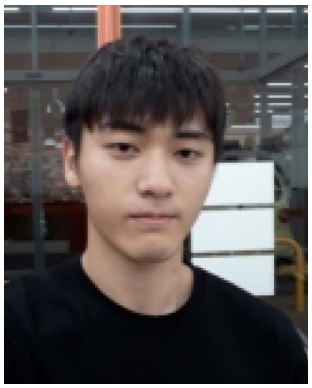

Jun Kim received a B.S. degree in chemical engineering from POSTECH (2017). Currently he is a PhD candidate in chemical engineering at POSTECH, Republic of Korea, under the supervision of Prof. Jin Kon Kim since 2017. His research interests include synthesis of mesoporous 3D graphene utilizing block copolymers and its application in energy storage systems.

Changshin Jo is an Assistant Professor at the Graduate Institute of Ferrous & Energy Materials Technology (GIFT) and the Department of Chemical Engineering at Pohang University of Science and Technology (POSTECH). He obtained his B.S. degree (2010) and PhD degree (2016) on synthesis of nanostructured electrode materials in the Department of Chemical Engineering at POSTECH. He then joined the University of Cambridge as a Research Associate and Marie Skłodowska-Curie Fellow (2017–2020) in the Department of Engineering. He also worked two years as an Assistant Professor in the Department of Chemical Engineering at Chung-Ang University (2020–2022). The main themes of his research in the NEDL group have been (i) synthesis of functional inorganic materials and (ii) applications of those materials in energy storage applications.

Jin Kon Kim is a full professor of Chemical Engineering at POSTECH. Also, he is the director of the Center for Smart Block Copolymer Self-Assembly funded by the National Creativity Research Initiative Program supported by the National Research Foundation in Korea. He received his B.S. in chemical engineering from Seoul National University (Korea) in 1980, M.S. in chemical engineering from Korea Advanced Institute of Science and Technology (Korea) in 1982, and PhD in chemical engineering from Polytechnic University in 1990. His research interests include phase behavior of block copolymers and development of new functional nanomaterials based on block copolymer self-assembly.

converted to mesoporous materials through post-treatments, such as calcination and solvent extraction.[64,73–98]

Because it enables tailoring of synthesis conditions, soft templating is a powerful synthetic approach capable of producing mesoporous materials with various compositions and morphologies. The properties of mesoporous materials play a vital role in determining the final performance; therefore, a number of synthetic approaches have been reported for tailoring various compositions (carbon,[84,99,100] metal oxide,[101,102] and metal-based materials[103,104]) and morphologies (hierarchical structures,[82,105,106] particles,[107,108] and patterned films[109–111]).

Herein, we focus on the recent developments in the mesoporous materials and their application to ESSs. In particular, the synthetic approaches and composition of carbon and metal-based materials (metal, metal oxide, and metal nitride) were covered, which have been intensively studied for ESSs. Following the introduction, the second section introduces the basic principles of synthetic approaches (hard and soft templating) for mesoporous materials. In the third section, various compositions of mesoporous materials prepared using the soft-templating method are reviewed. The fourth section discusses soft-templating methods for synthesizing various hierarchical architectures composed of mesoporous structures. The fifth section presents the potential applications of mesoporous materials in batteries and supercapacitors. Finally, the summary and perspective of the soft-templating method are described.

2. Synthetic approaches for mesoporous materials

Several synthetic approaches have been reported for preparing mesoporous materials with various compositions, such as metals, metal oxides, metal nitrides, and carbon.[143–163] In general, the condensation and crystallization reactions of most precursors proceed in random directions to form a micrometer-scale bulk structure. Therefore, the morphological changes in most materials during the reaction are difficult to predict, thus limiting nano-scale structural control.[112–115] To solve this issue, hard-template and soft-template methods that can maintain the mesoporous structure during the reaction of precursors have been proposed.[116–119]

Hard-templating methods use thermally stable templates such as pre-synthesized mesoporous silica, carbon, and metal oxide-based nanocrystals (Fig. 1a). To obtain mesoporous materials, the reaction proceeds upon heat treatment after the hard template is filled with the precursors. Owing to the thermally stable hard template, the reaction can be terminated without structural collapse even at high temperatures,[106,120–123] resulting in high-quality mesoporous materials having highly crystallinity and even single-crystallinity.[70,71] However, this method has the disadvantages of being a time-consuming process and costly, because an additional process is required to prepare the sacrificial template. In the process of removing the sacrificial template, the use of a corrosive solvent is unavoidable, which is non-environment friendly and even harmful. In addition, it is difficult to control the pore size/shape because the resultant product is the inverted shape of the sacrificial template.

Meanwhile, soft-templating has been regarded as a powerful synthetic approach for mesoporous materials because this method enables efficient control of mesoporous materials in a short time through the co-assembly of a SDA and precursors to form mesostructured composites (Fig. 1b). Here, SDAs act as both the structure-directing agent and the soft template. When

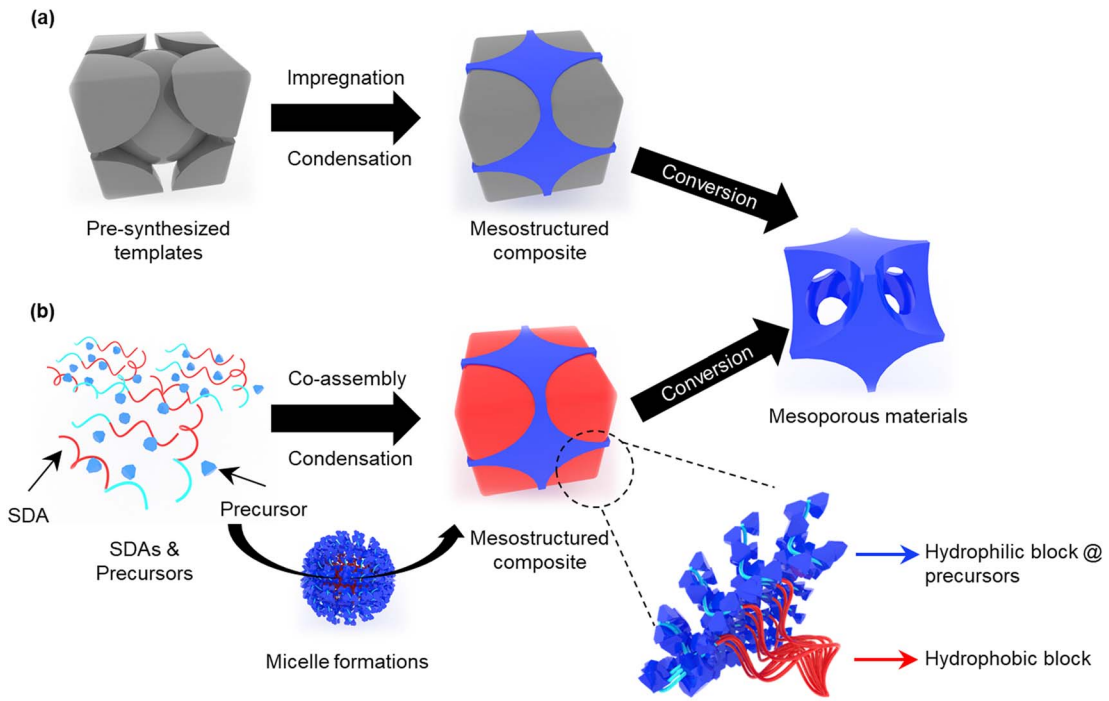

Fig. 1 Schematic of (a) hard- and (b) soft-templating methods for fabricating mesoporous materials.

a solution containing SDAs and precursors evaporates and reaches a concentration higher than the critical micelle concentration, the SDAs and precursors start self-assembling into spherical or cylindrical micelles. After the solvent completely evaporates, a mesostructured composite is formed. This process is called evaporation-induced self-assembly (EISA).[124–128] When hydrophilic precursors are used, the obtained mesostructured composite consists of a stack of micelles in which the hydrophobic and hydrophilic parts containing the precursors are separated. After the template is removed (mainly by calcination), the hydrophilic and hydrophobic parts were converted into a skeleton and mesopores, respectively. The soft templating method can produce mesoporous materials with various compositions and morphologies by adjusting the precursors and molecular structures of the SDAs (Fig. 2). Despite their high flexibility and universal applicability, many parameters should be considered for soft-templating. Also, their structural stability and crystallinity are lower than those synthesized by hard-templating methods. For instance, co-assembly of SDAs and precursors requires sensitive synthesis conditions (*e.g.*, precursor reactivity control, appropriate humidity, solvent composition, *etc.*), and collapse of the mesoporous structure often occurs during the template removal process. Therefore, many efforts have been made to address the above issues, which will be discussed in detail in the following section.

3. Soft-template synthesis of mesoporous materials with various compositions

The soft-template synthetic process is divided into two steps: (i) formation of a mesostructured composite through micelle formation and (ii) conversion from a mesostructured composite to mesoporous materials by eliminating SDAs. During the formation of a mesostructured composite (step (i)), suitable SDAs should be chosen. Small-molecule surfactant SDAs are inexpensive and soluble in both water and organic solvents, enabling the easy synthesis of mesoporous materials. However, their low molecular weight limits the pore size control. Meanwhile, BCPs have easily controllable lengths of hydrophilic and hydrophobic blocks; thus, the pore size and wall thickness can be finely tuned. The most commonly used BCPs as SDAs comprise both hydrophilic and hydrophobic blocks. Poly(ethylene oxide) (PEO), poly(2-vinylpyridine) (P2VP), and poly(4-vinylpyridine) (P4VP) have been widely used as hydrophilic blocks, whereas poly(propylene oxide) (PPO), polystyrene (PS), poly(isoprene) (PI), and poly(butadiene) (PB) are used as hydrophobic blocks.[129–133] During step (ii), mesoporous materials are obtained by removing the SDA (mainly using heat treatment) and improving the mechanical strength of the components. Because SDAs with small molecular weights have

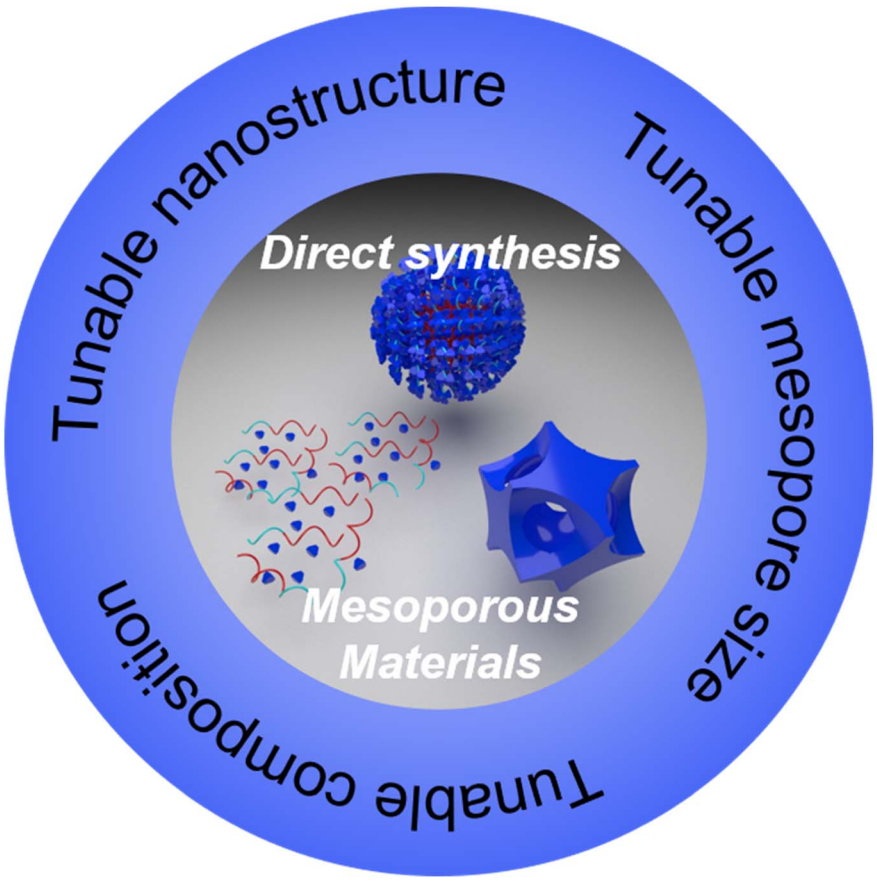

Fig. 2 Synthetic versatility of mesoporous materials based on the soft-templating method.

Table 1 Summary of mesoporous materials synthesized by the soft-templating method

Product	Template	Solvent	Precursor	Pore size (nm)	S_{BET} ($m^2\ g^{-1}$)	Ref.
Mesoporous carbon	PEO-*b*-PPO-*b*-PEO	EtOH	Resol	6.8	590.0	146
Mesoporous polymer–silica and carbon–silica nanocomposites	F127	EtOH/HCl	Tetraethyl orthosilicate/resol	6.7	2470.0	147
Mesoporous carbon	PS-*b*-PEO	THF	Resol	23.0	1510.0	117
Mesoporous carbon	PAN-*b*-PMMA	—	PAN-*b*-PMMA	5.96–17.42	427.6–213.1	28
N and O dual-doped mesoporous carbon	PAN-*b*-PMMA	DMF	PAN-*b*-PMMA	10.0	503.0	26
N-Doped mesoporous carbon	PS-*b*-PAA	THF/H_2O	Urea–formaldehyde	9.5–17.2	458.0–476.0	29
Mesoporous TiO_2	PI-*b*-PEO	THF	Titanium chloride	23.6	75.0	137
Mesoporous TiO_2	PS-*b*-PEO	THF	Titanium isopropoxide/titanium chloride	20.7	72.0	162
Mesoporous TiO_2	PS-*b*-PEO	THF/AcAc	Titanium isopropoxide	16.0	112.0	68
Mesoporous TiO_2	PS-*b*-P2VP-*b*-PEO	THF/HCl	Titanium isopropoxide	35.0–45.0	90.0	89
Mesoporous Nb_2O_5	PI-*b*-PEO	Chloroform	Niobium chloride/niobium ethoxide	24.0	69.0	137
Mesoporous CoO_x/C	PS-*b*-PEO	THF	Cobalt nitrate hexahydrate/resol	13.4–16.0	394.0–483.0	165
Mesoporous WO_3	PS-*b*-PEO	THF/AcAc	Tungsten chloride	10.6–15.3	76.0–136.0	166
Mesoporous $TiNb_2O_7$	PS-*b*-PEO	THF/HCl	Titanium isopropoxide/niobium ethoxide/tetraethyl orthosilicate	40.0	74.0	155
Mesoporous $Ce_xZr_{1-x}O_2$	PS-*b*-PEO	THF/EtOH	Zirconium acethylacetonate/cerium chloride heptahydrate	10.6–15.1	65.8–73.7	156
Mesoporous Fe_2O_3	PS-*b*-PAA-*b*-PEG	THF/NaOH	Iron nitrate nonahydrate	39.0	86.9	177
Mesoporous Pt	PI-*b*-PDMAEMA	Chloroform/Methanol	Stabilized Pt	17.0	18.0	192
Mesoporous Au	PS-*b*-PEO	—	Gold chloride trihydrate	20.0–60.0	—	194
Mesoporous Rh	PMMA-*b*-PEO	DMF/H_2O	Sodium hexachlororhodate/ascorbic acid	9.0	50.0	193
Mesoporous TiN–C	F127	$EtOH/H_2O$	$TiCl_4$/resol	8.0	389.0	37
Mesoporous TiN	PI-*b*-PS-*b*-PEO	THF/HCl	Pt	18.8	60.0	206
Mesoporous NbN	PI-*b*-PS-*b*-PEO	THF/HCl	Pt	26.8	49.0	206

poor thermal stability, structural collapses often occur during high-temperature calcination. Meanwhile, BCPs can enhance thermal stability depending on the type of block, and an ordered mesoporous structure can be maintained without structural collapse even after calcination at high temperatures. Under these considerations, BCP-based SDAs can maintain structural stability even at high temperatures, enabling the synthesis of mesoporous carbon and metal oxides, as well as metal nitrides that require an additional high-temperature nitridation process. Compared to other compositions, mesoporous metals require a complementary soft-templating method because of their high surface energy and difficulty in co-assembling precursors and SDAs. In this section, we focus on synthetic approaches for mesoporous carbon, metal oxides, metals, and metal nitrides. The mesoporous materials covered in this review are summarized in Table 1.

3.1. Carbon-based materials

Mesoporous carbons have been widely used as catalysts,[134–136] fuel cells,[53,137,138] and energy storage devices[40,139–141] owing to their high surface area, light weight, and excellent thermal and chemical stability.[142–145] To synthesize mesoporous carbon using the soft-template method, the following conditions must be satisfied. First, a mesostructured composite should be formed through the co-assembly of the carbon precursors and SDAs; for this purpose, low molecular weight precursors should be used. Second, during high-temperature heat treatment to convert the mesostructured composite to mesoporous carbon, the SDAs must be thermally decomposed through carbonization, while the precursors should retain their structure. Therefore, the selection of precursors and SDAs should be carefully considered.

Meng *et al.* first demonstrated the synthesis of mesoporous carbon using the soft template method.[146] They used PEO-*b*-PPO-*b*-PEO as an SDA and low-molecular-weight polymers made of phenol and formaldehyde as a precursor. As the solvent evaporated from the solution containing the SDAs and precursor, an ordered mesostructured composite was formed. Here, the low-molecular-weight polymer can interact selectively with the PEO block to successfully form a mesostructured composite. In the mesostructured composite, a thermally stable resol resin was formed *via* thermopolymerization at a relatively low temperature (100–140 °C). During the conversion process at high temperatures (350–500 °C), the resol resin stably maintained the carbon framework, while the SDA thermally decomposed, yielding mesoporous carbon. The obtained mesoporous carbon had pore diameters of 6.8 nm, as well as large surface area (590 $m^2\ g^{-1}$) and pore volume (0.51 $cm^3\ g^{-1}$). Although mesoporous carbon can be synthesized using this approach, the carbonization process induces structural shrinkage accompanied by a decrease in pore size, pore volume, and surface area. To solve this problem, Liu *et al.* proposed a triconstituent co-assembly approach.[147] First, they prepared mesostructured composites using a silicate oligomer, PEO-PPO-PEO, and resol. Silicate served as a reinforcing material to relieve structural shrinkage during calcination. Framework shrinkage after calcination was minimized because of the presence of rigid silicates. For instance, large pore sizes reaching 8.5 and 6.7 nm for the mesostructured composite and for carbon–silica nanocomposite, respectively, were achieved. After removing the silica using an HF solution, ordered mesoporous carbon with a pore size of 6.7 nm, pore volume of 2.02 $cm^3\ g^{-1}$, and large surface area of 2470 $m^2\ g^{-1}$ was obtained. In addition to the original pores, small pores generated by the removal of silica contribute to the large surface area. Based on these approaches, many researchers have synthesized mesoporous carbons.[131–138] However, the pore size is still limited to less than 10.0 nm because of the low molecular weight of Pluronic SDAs, which greatly limit their applications. Instead of using Pluronic SDAs, Deng *et al.* synthesized mesoporous carbon using PS-*b*-PEO as an SDA and low-molecular-weight resol as a carbon source.[117] To increase the pore size, they synthesized PS-*b*-PEO with a larger molecular weight (PS_{230}-*b*-PEO_{125}, 29 700 g mol^{-1}) than Pluronic F127 (12 600 g mol^{-1}). When the solvent evaporated from the solution containing resol and PS-*b*-PEO, co-assembly of resol and PEO occurred to form a mesostructured composite. The resultant mesoporous carbon had a relatively large pore size (~23.0 nm) because of the high molecular weight of PS-*b*-PEO.

Yan *et al.* reported a new synthetic approach for mesoporous carbon (Fig. 3a).[28] Here, many parameters for co-assembly kinetics, such as the ratio of SDAs and carbon source and solvent evaporation rate, can be ignored because the soft template served as the carbon source. They utilized polyacrylonitrile-*b*-polymethylmethacrylate copolymer (PAN-*b*-PMMA) as both the carbon precursor and SDAs. PAN and PMMA served as carbon sources and sacrificial blocks, respectively. PAN-*b*-PMMA self-assembled through microphase separation to form a mesostructure at 250 °C and then converted to mesoporous carbon after subsequent carbonization at 800 °C. Then, PAN was converted to carbon, and PMMA was thermally decomposed to form mesopores. During thermal treatment at 250 °C, PAN remained thermally stable throughout the cross-linking reactions accompanied by partial dehydrogenation and cyclization of PAN (Fig. 3b). After carbonization, PAN-*b*-PMMA was converted to mesoporous carbon without structural collapse because the cross-linking of PAN offered sufficient thermal stability. Furthermore, the pore size was precisely controlled by adjusting the molecular weight or volume fraction of the sacrificial PMMA block.[26,148–151] Recently, Zhou *et al.* demonstrated the synthesis of mesoporous carbon fibers by electrospinning PAN-*b*-PMMA with 64 vol% PAN (Fig. 3c).[26] During electrospinning, the solvent rapidly evaporated, resulting in the formation of fibers. The oxidation process then stabilized the fiber structure through the crosslinking and cyclization of PAN. After pyrolysis, the fiber maintained its shape without agglomeration and exhibited a bicontinuous mesoporous structure (Fig. 3d and e).

Considerable effort has been focused on fabricating heteroatom-doped (such as N, B, P, O, and S) mesoporous carbons, particularly N-doping because N atoms can significantly enhance the wettability, surface polarity, electrical conductivity, and electron-donor affinity of carbon

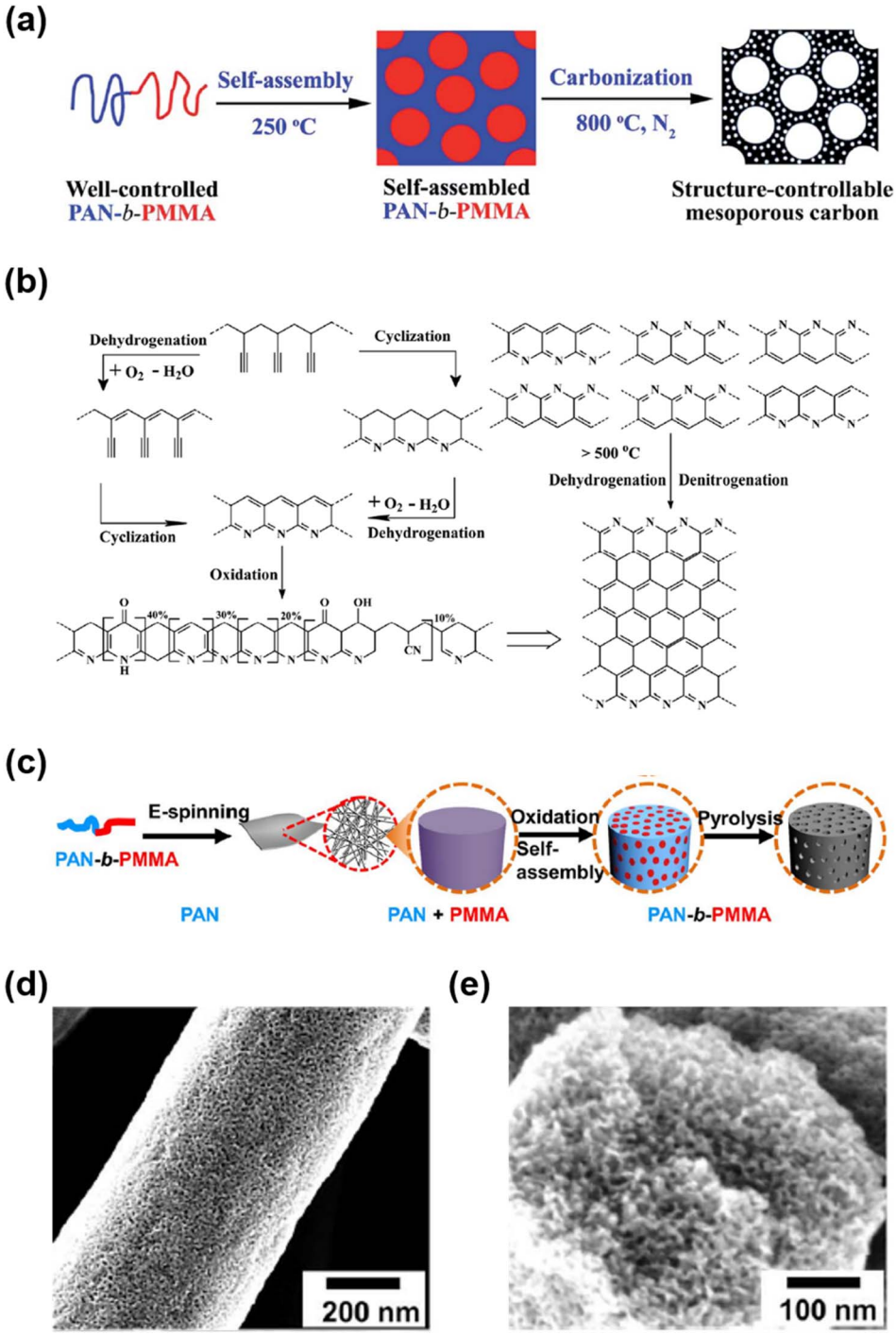

Fig. 3 (a) Conversion process of PAN-*b*-PMMA into mesoporous carbon. (b) Mechanism of thermal chemistry of PAN carbonization: (left) thermal stabilization and (right) pyrolysis involving dehydrogenation and denitrogenation, which eventually lead to the partially graphitic structure.[28] Copyright 2015, Royal Society of Chemistry (c) fabrication of the mesoporous carbon fiber. (d and e) SEM images of the mesoporous carbon fiber.[26] Copyright 2019, The American Association for the Advancement of Science.

frameworks.[134,152,153] Carbonization of organic self-assembled composites comprising SDAs and certain N-containing precursors (such as melamine, urea–phenol–formaldehyde resins and dicyandiamide) provides a versatile route for synthesizing N-doped mesoporous carbon.[8,67] However, retaining the structural stability of the resulting mesoporous carbons requires a small amount of N-rich dopants, which greatly restricts the final N content in the framework. To overcome this limitation, Liu *et al.* reported a new synthetic route for rich N-doped mesoporous carbons based on a template-catalyzed *in situ* polymerization and co-assembly process.[29] They used polystyrene-*b*-poly(acrylic acid) copolymer (PS-*b*-PAA) as the SDA, and catalyst

and urea–formaldehyde (UF) precursors as both the carbon and nitrogen sources. The proposed mechanism is illustrated in Fig. 4. When PS-*b*-PAA, formaldehyde, and urea were dissolved in a THF/H_2O solution, hydrogen ions were generated from the PAA block owing to ionization in water, thereby catalyzing the polymerization of UF to form UF precursors through hydroxymethylurea derivatives. As THF evaporated, the amount of H_2O in the solution increased, resulting in spherical PS-*b*-PAA micelles, in which PS and PAA formed the core and shell, respectively. The UF precursors interact with the PAA block to form a UF precursor/PS-*b*-PAA composite. After all of the solvent evaporated, cross-linking of UF precursors occurred to form UF resin/PS-*b*-PAA, which was converted into N-rich mesoporous carbon *via* subsequent pyrolysis in nitrogen. Because the N-rich

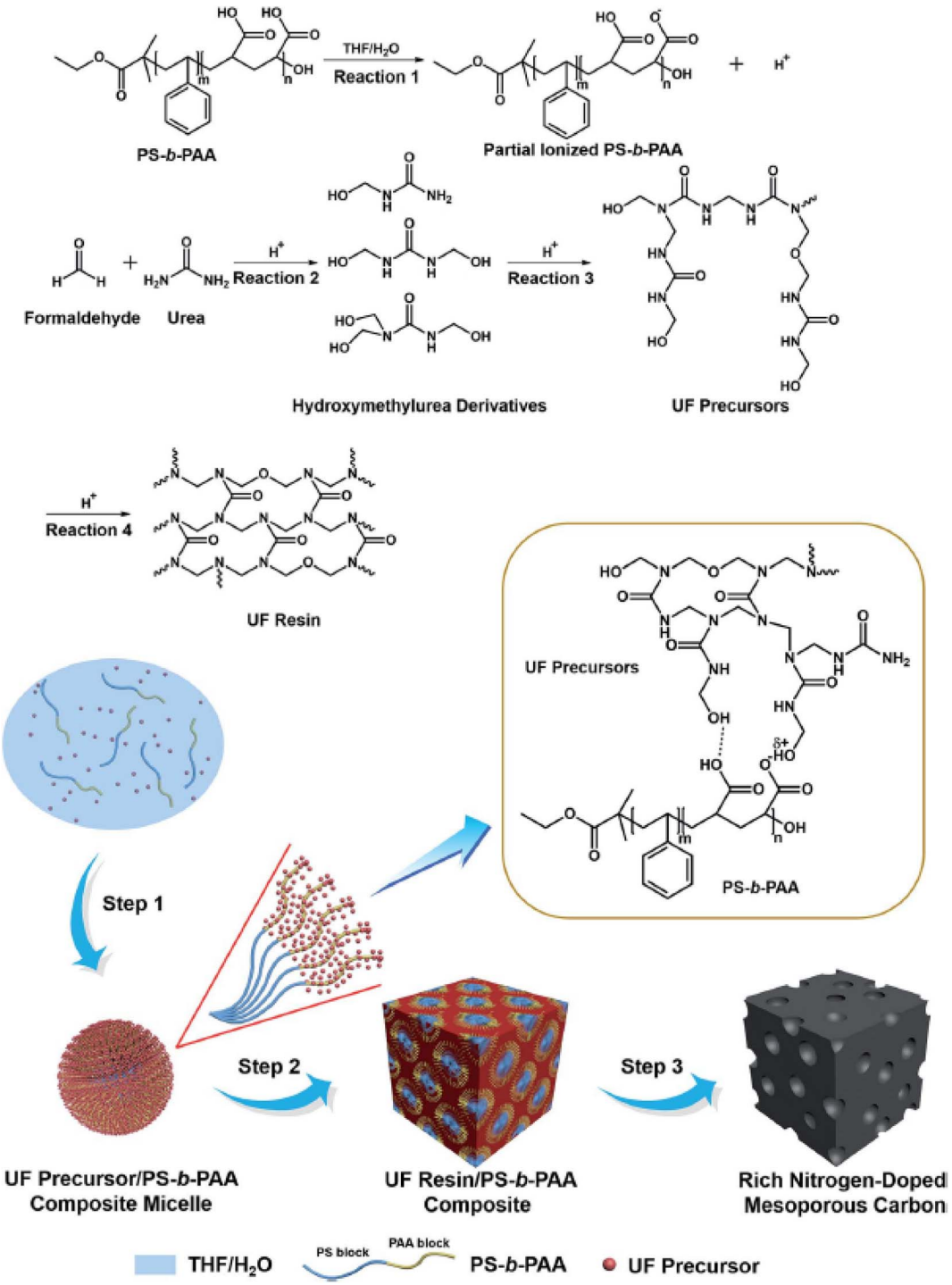

Fig. 4 The formation of rich N-doped mesoporous carbon through a template-catalyzed *in situ* polymerization and co-assembly process.[29] Copyright 2018, Royal Society of Chemistry.

UF resin was used as the main framework in the composites, the obtained mesoporous carbon had a high N content (~19 wt%).

3.2. Mesoporous metal oxides

Mesoporous metal oxides, especially transition metal oxides, have received considerable interest because of their intrinsic physicochemical properties, high surface area, and wide range of applications in energy storage materials,[154,155] sensors,[92] and catalysts.[156] In synthesizing mesoporous metal oxides, the thermal stability of the soft template, reactivity to hydrolysis and condensation of inorganic precursors, and crystallization of metal oxides should be considered.[157,158]

Block copolymer-based SDAs have been widely employed as soft template materials for the synthesis of mesoporous metal oxides. The presence of water induces explosive hydrolysis and condensation of precursors, which cause difficulty in co-assembly with SDAs. Therefore, the co-assembly of the SDA and precursors in a nonaqueous solution is required. Yang *et al.* demonstrated a general procedure for synthesizing mesoporous metal oxides.[159,160] They synthesized ordered mesoporous metal oxides, including TiO_2, ZrO_2, Nb_2O_5, Ta_2O_5, Al_2O_3, SnO_2, WO_3, HfO_2, and their mixed oxides, using non-aqueous solutions containing metal chloride precursors and poly(alkylene oxide) containing BCPs (for instance, Pluronic). The pore walls of the obtained metal oxides were semi-crystalline and most metal oxides exhibited hexagonally packed mesophases. Although Pluronic has been widely used to synthesize mesoporous metal oxides, tunable pore sizes and highly crystalline phases are difficult to obtain owing to its low molecular weight and low thermal stability.[159,160] Fattakhova-Rohlfing *et al.* reported the differences between TiO_2 synthesized from Pluronic and non-Pluronic SDAs.[80] They used P123, and poly(ethylene-*co*-buthylene)-*b*-poly(ethylene oxide) copolymer (KLE) as Pluonic and non-Pluronic SDAs, respectively. Mesoporous TiO_2 obtained from KLE showed high crystallinity and maintained its mesoporous structure in the temperature range of 550–700 °C. By contrast, mesoporous TiO_2 derived from P123 exhibited a collapsed mesoporous structure at 600 °C. This difference is attributed to the large molecular weight of KLE, which provides mesoporous TiO_2 with thicker pore walls that can sufficiently support the mesostructures during calcination. Therefore, block copolymers with high molecular weights are suitable for producing crystalline mesoporous metal oxides because of high thermal stability owing to their large molecular weights. In addition, tailored pore sizes can be obtained by adjusting the volume ratio of the hydrophilic/hydrophobic blocks and molecular weight.

Although crystalline mesoporous metal oxides can be synthesized using non-Pluronic SDAs, certain metal oxides with high crystallization temperatures are still difficult to synthesize because crystallization and template decomposition simultaneously occur during calcination. Early template decomposition causes structural collapse; therefore, a thermally stable template at high temperature is required for the synthesis of highly crystalline mesoporous metal oxides.[161] Lee *et al.* introduced the combined assembly by soft and hard (CASH) method to achieve highly crystalline mesoporous metal oxides with large-sized and uniform pores without structural collapse (Fig. 5a).[137] They used PI-*b*-PEO as the SDA. A hydrophilic PEO block was easily decomposed upon heating and the hydrophobic PI block containing sp^2 carbon was converted to a thermally stable amorphous carbon during thermal treatment in an inert (argon) environment. During this process, PEO was burned off, and the metal oxide crystals nucleated, grew, and were sintered into the wall material. Simultaneously, the PI block was converted to amorphous carbon, which can sufficiently support the mesoporous structure. The remaining amorphous carbon was removed by heating in air, and highly crystalline mesoporous metal oxides were thus obtained. Owing to the thermally stable amorphous carbon, the mesoporous metal oxides could be maintained without structural collapse, even at 1000 °C. Highly crystalline mesoporous TiO_2 (Fig. 5b and c) and Nb_2O_5 (Fig. 5d and e) that crystallized at temperatures higher than 400 °C were synthesized. Notably, the CASH method can be extended to other polymers containing sp^2 carbons; therefore, thermally stable mesoporous TiO_2 and Nb_2O_5 were synthesized using PS-*b*-PEO.[162]

The CASH method has been reported to be capable of stable conversion from composite to crystalline mesoporous metal oxides; however, the synthesis of certain mesoporous metal oxides with high reactivity to hydrolysis and condensation under non-hydrolytic sol–gel conditions remains difficult because solvent purity and relative humidity can affect the hydrolysis and condensation reactions of inorganic precursors, resulting in poor reproducibility of the co-assembly of inorganic precursors and SDAs.[163] To solve this problem, Zhang *et al.* reported a novel ligand-assisted assembly method for preparing highly ordered crystalline mesoporous metal oxides (Fig. 5f).[68] To control the hydrolysis and condensation of inorganic precursors, they employed acetylacetone (AcAc) as a coordination agent. AcAc interacted with the highly reactive titanium isopropoxide to retard the hydrolysis and condensation reactions, which increased the time for precursors to co-assemble with SDAs. Therefore, the co-assembly process was more controllable, leading to highly ordered and crystalline mesoporous TiO_2 after calcination (Fig. 5g–j).

Based on the above two methods, various mesoporous metal oxides have been synthesized.[88,89,164–166] Zhu *et al.* synthesized highly ordered mesoporous WO_3 using ligand-assisted co-assembly to prepare a mesostructured composite and the CASH method to convert it to mesoporous oxides (Fig. 6a).[166] They used PS-*b*-PEO, WCl_6, and AcAc as the soft template, inorganic precursor, and chelating agent, respectively. AcAc strongly coordinates with tungsten ions and retards hydrolysis and thus can stabilize the co-assembly of the SDA and precursors. The co-assembled composite was then heated under a nitrogen atmosphere. Owing to the thermally stable amorphous carbon derived from the PS block, structural collapse was prevented during the high-temperature crystallization process. After calcination in air to remove residual carbon, ordered crystalline mesoporous WO_3 was obtained. In addition, by using PEO-*b*-PS with different volume fractions of PEO, mesopores of various sizes were obtained (Fig. 6b–e). In addition, molecules

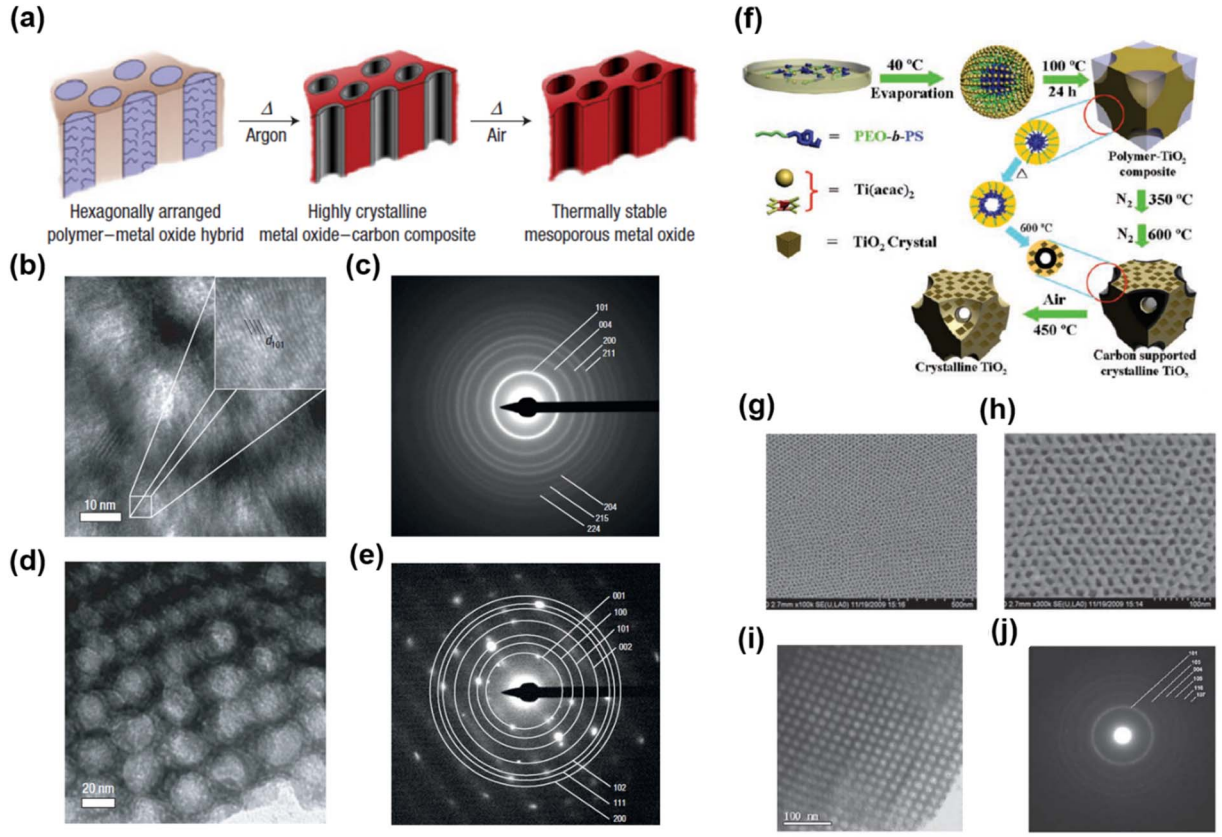

Fig. 5 (a) Schematic of the CASH method. HR-TEM images and SAED patterns of mesoporous TiO_2 (b, c) and Nb_2O_5 (d and e).[137] Copyright 2008, Springer Nature. (f) Process of forming ordered and highly crystallized large-pore mesoporous TiO_2 from the ligand-assisted assembly method. FESEM (g, h) and TEM (i) images of mesoporous TiO_2 and its corresponding SAED pattern (j).[68] Copyright 2011, Wiley-VCH.

capable of coordinating with metal ions have been used as chelating agents, such as polyols, amines, resol, and α-hydroxycarboxylic acids including ascorbic, lactic, citric, or glycolic acids.[167–170] Another approach to controlling the reaction rate of the precursors is by using acidic conditions. Under highly acidic conditions, the hydrolysis of metal alkoxide precursors is accelerated, but condensation is hindered due to the protonation of M − OH moieties.[155,171–173] In addition, the inverse of condensations is also promoted. These effects lead to the formation of small hydrophilic oligomers, thus providing a stable co-assembly with SDAs without chelating agents.[173] Jo *et al.* synthesized mesoporous $TiNb_2O_7$ under highly acidic conditions.[155] To control the condensation rate of precursors, they added an appropriate amount of concentrated HCl (35–37%) to a mixture of Ti and Nb-alkoxide (here, $[H_2O/M(OR)_x] > 2$). At a controlled condensation rate, the Ti and Nb sols were controlled to a small size that could sufficiently interact with the PEO block of PS-*b*-PEO. After mesostructured composite formation and subsequent calcination, ordered mesoporous $TiNb_2O_7$ was synthesized.[155] The versatile soft-template processes enabled the synthesis of various mesoporous metal oxides in single and multiple compositions, as well as nanoparticle-decorated metal oxides.[101,174–182] Recently, Yang *et al.* reported the synthesis of multi-composition and nanoparticle-decorated mesoporous metal oxides (Fig. 6f).[156] They prepared precisely controlled mesoporous $Ce_xZr_{1-x}O_2$ ($0 < x < 1$) by tuning the Ce/Zr molar ratio of the feeding precursors. In addition, Pt nanoparticles were decorated on the surface of mesoporous $Ce_xZr_{1-x}O_2$ through the *in situ* reduction of an $H_2PtCl_6 \cdot 6H_2O$ aqueous solution by $NaBH_4$ (Fig. 6g–i).

Despite these significant advances in the synthesis of mesoporous metal oxides, some metal oxides such as CoO_3, MoO_3, and V_2O_5 are still difficult to synthesize into high-quality mesoporous structures because of their rapid thermal growth at high temperatures and requirement of multiple oxidation states. Lunkenbein *et al.* reported several strategies for template removal from the mesostructured composite to synthesize mesoporous MoO_3 (Fig. 7).[81] The composite comprised poly(-butadiene)-*b*-poly(dimethylaminoethyl methacrylate) copolymer (PB-*b*-PDMAEMA) as a soft template and phosphomolybdic acid ($H_3PMo_{12}O_{40}$) as a MoO_3 precursor. They employed three methods to remove SDAs from the mesostructured composites: (1) direct calcination, (2) CASH method, and (3) sequential heat and H–O-plasma treatments. In the first method, direct calcination induced both the fast growth of MoO_3 nanocrystals and template decomposition, resulting in agglomerated crystalline MoO_3. In the second method, the mesostructured composite was subjected to heat treatment in an inert environment and subsequently calcined in air. The composite heat-treated in an inert environment maintained

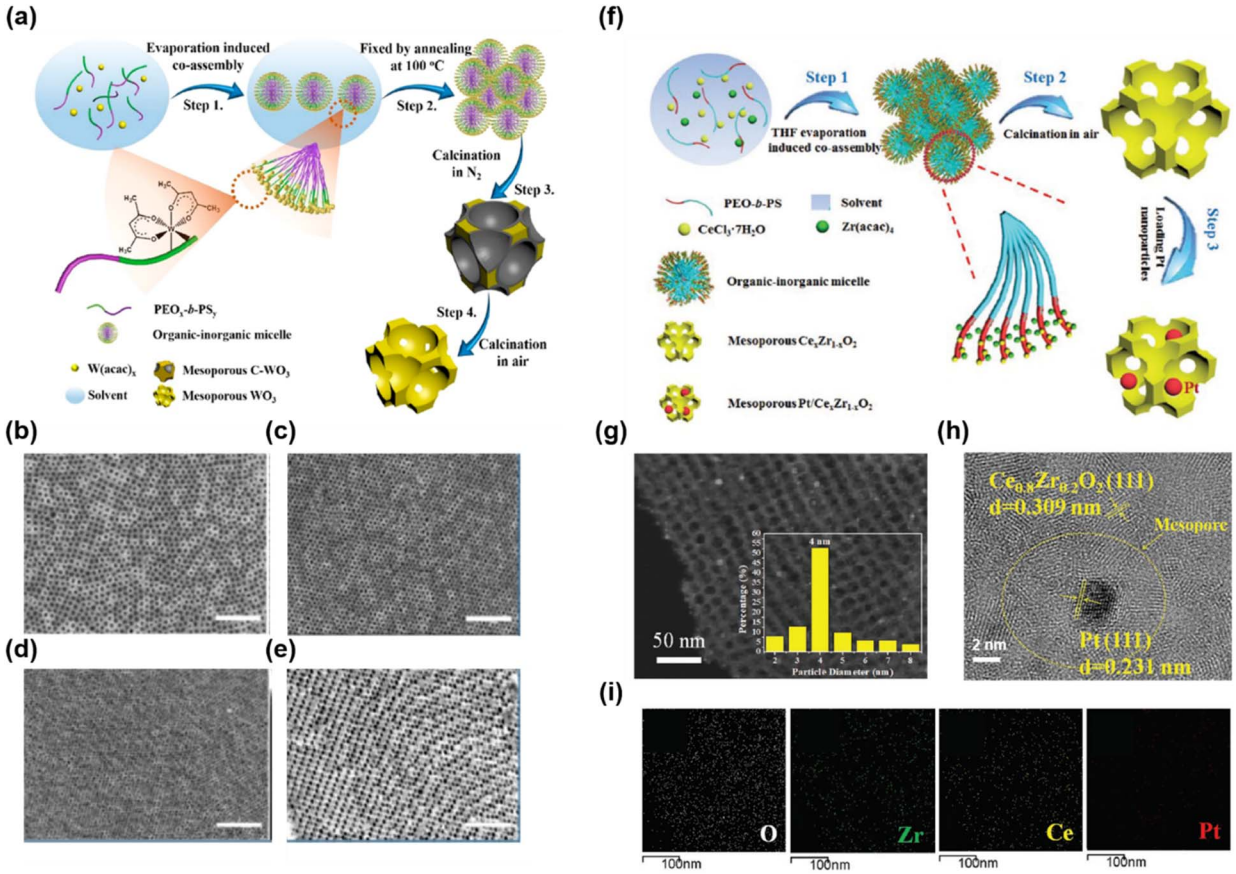

Fig. 6 (a) Schematic of the formation of ordered mesoporous WO_3 *via* ligand-assisted co-assembly and the subsequent CASH method. (b–e) FESEM images of mesoporous WO_3 with two different pore sizes. (b and d: top view and c and e: cross-sectional view)[166] Copyright 2017, American Chemical Society. (f) The synthesis process of ordered mesoporous $Ce_xZr_{1-x}O_2$ and Pt/$Ce_xZr_{1-x}O_2$. (g) STEM and (h) HR-TEM images, and (i) energy-dispersive X-ray element mapping of O, Zr, Ce, and Pt in Pt/$Ce_xZr_{1-x}O_2$.[156] Copyright 2019, Wiley-VCH.

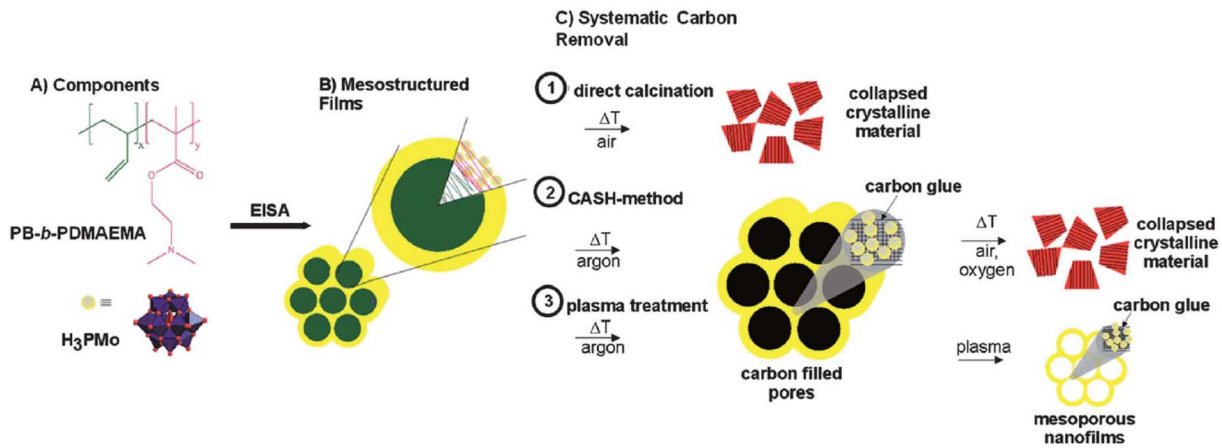

Fig. 7 (a) Chemical structures of H_3PMo and PB-*b*-PDMAEMA. (b) H_3PMo clusters were selectively incorporated into the PDMAEMA domains. (c) Systematic calcination studies were conducted either directly in air (route 1) or by applying a two-step heat treatment (route 2): first in an argon atmosphere and second in an oxidative atmosphere. Alternatively, argon heat-treated samples were exposed to H–O plasma (route 3).[81] Copyright 2013, Royal Society of Chemistry.

a mesoporous structure; however, the structure collapsed after the subsequent heat treatment to remove the template because of the change in the oxidation state of Mo. During heat treatment in an inert environment, the oxidation state of Mo was reduced because of its low oxygen fugacity. During heat treatment in air to remove carbon, the MoO_3 crystal, which

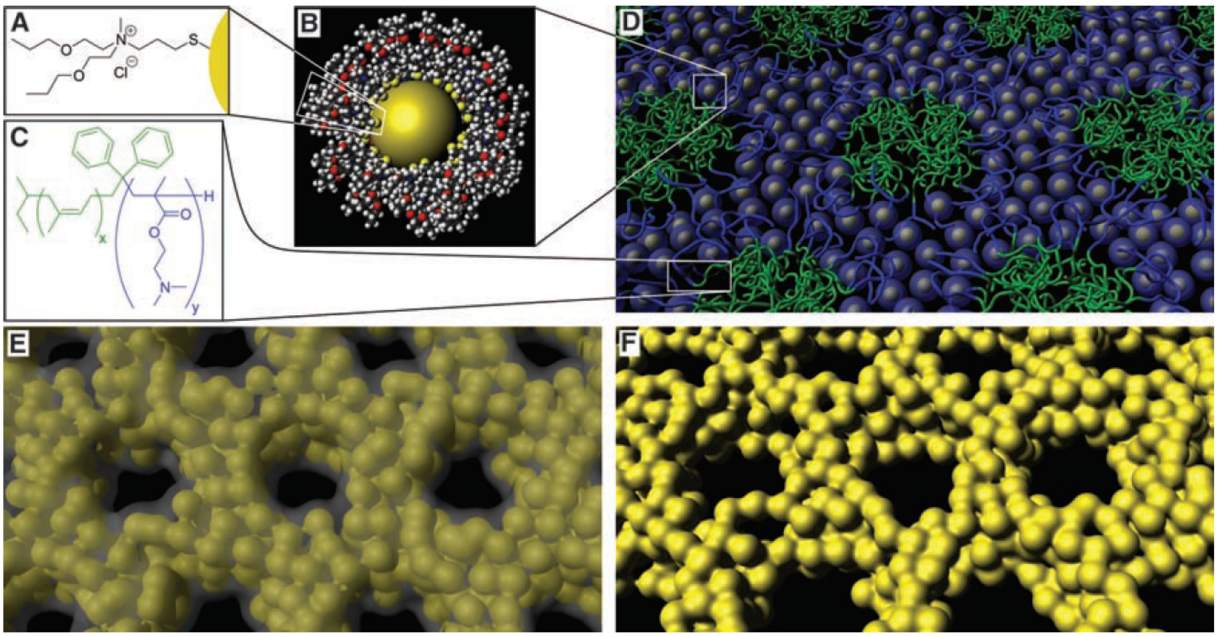

Fig. 8 (a) Chemical structure of the ligand used to produce moderately hydrophilic Pt NPs with high solubility. (b) A true-scale model of a NP. (c) Chemical structure of PI-*b*-PDMAEMA. (d) Self-assembly of Pt NPs with the block copolymer. (e) Pyrolysis of the mesostructured composite under an inert atmosphere produces a mesoporous Pt–C composite. (f) Ar–O plasma treatment or acid etching of Pt–C produces ordered mesoporous Pt.[192] Copyright 2008, The American Association for the Advancement of Science.

contained the highest oxidation state of Mo, rapidly grew, leading to the collapse of the mesoporous structure. In the third method, a mesoporous structure was obtained by subjecting the mesostructured composite to heat treatment in an inert environment and subsequent H–O-plasma treatment; however, the carbonaceous material still remained. Therefore, new methods (or strategies) for synthesizing mesoporous metal oxides in multiple oxidation states are needed.

3.3. Metals

Metallic materials exhibit distinctive physicochemical characteristics, such as inherent conductivity and electrochemical stability.[183,184] Mesoporous metal structures show enhanced performance in catalysis, energy conversion and storage, and chemical and biological sensors by maximizing the rate of electron transfer inside a porous structure.[185–187] Despite these advantages, the synthesis of mesoporous metallic materials remained a challenge for a long time owing to their high surface energies, which tend to minimize the surface area.[188,189] To fabricate mesoporous metallic materials, various strategies based on soft templates have been developed.[180–185]

To promote the self-assembly of metal nanoparticles (NP) and soft templates, the high surface energy of NPs should be reduced by capping them with ligand molecules.[190,191] Warren *et al.* successfully synthesized mesoporous Pt *via* the co-assembly of ligand-stabilized Pt NPs and a block copolymer (Fig. 8).[192] To synthesize mesoporous Pt, a specific block copolymer that meet the following requirements should be selected. First, NPs should be highly soluble in organic solvents to interact with the block copolymer. Second, ligand-stabilized NPs should possess a high metal volume fraction to prevent structural collapse during template removal. Third, the NPs should interact with only one block of the block copolymer. Fourth, the diameter of the NPs should be less than the microdomain size of the block to facilitate their incorporation into the target microdomain. They selected *N*,*N*-di-2-propoxyethyl-*N*-3-mercaptopropyl-*N*-methylammonium chloride as the ligand and PI-*b*-poly(dimethylaminoethyl methacrylate) copolymer (PI-*b*-PDMAEMA) as the SDA. The ligand-stabilized Pt NPs had a diameter of 1.4 nm and high solubility in organic solvents even after sufficient aging. Therefore, a macroscopically homogeneous solution was prepared by combining Pt NPs, PI-*b*-PDMAEMA, and a mixed solvent of chloroform and methanol. During solvent evaporation, the co-assembly of aged Pt NPs and PI-*b*-PDMAEMA occurred, leading to an ordered mesostructured composite which was finally converted to pure mesoporous Pt after Ar–O plasma treatment. Owing to the high metal content of the aged Pt NPs, ordered mesoporous Pt was successfully synthesized from the mesostructured composite without structural collapse. Li *et al.* successfully extended a single mesoporous metal to a binary mesoporous metal system *via* co-assembly of ligand-stabilized metal NPs and SDAs.[193]

Yamauchi's group suggested facile synthetic approaches yielding mesoporous metal films and NPs by combining a soft-templating method with electrochemical deposition (Fig. 9a–d)[194] or wet chemical synthesis (Fig. 9e–i).[195] The combination of soft templating and electrochemical deposition enabled the synthesis of a mesoporous metal film on a conductive substrate (Fig. 9a). They first prepared a soft-template film composed of

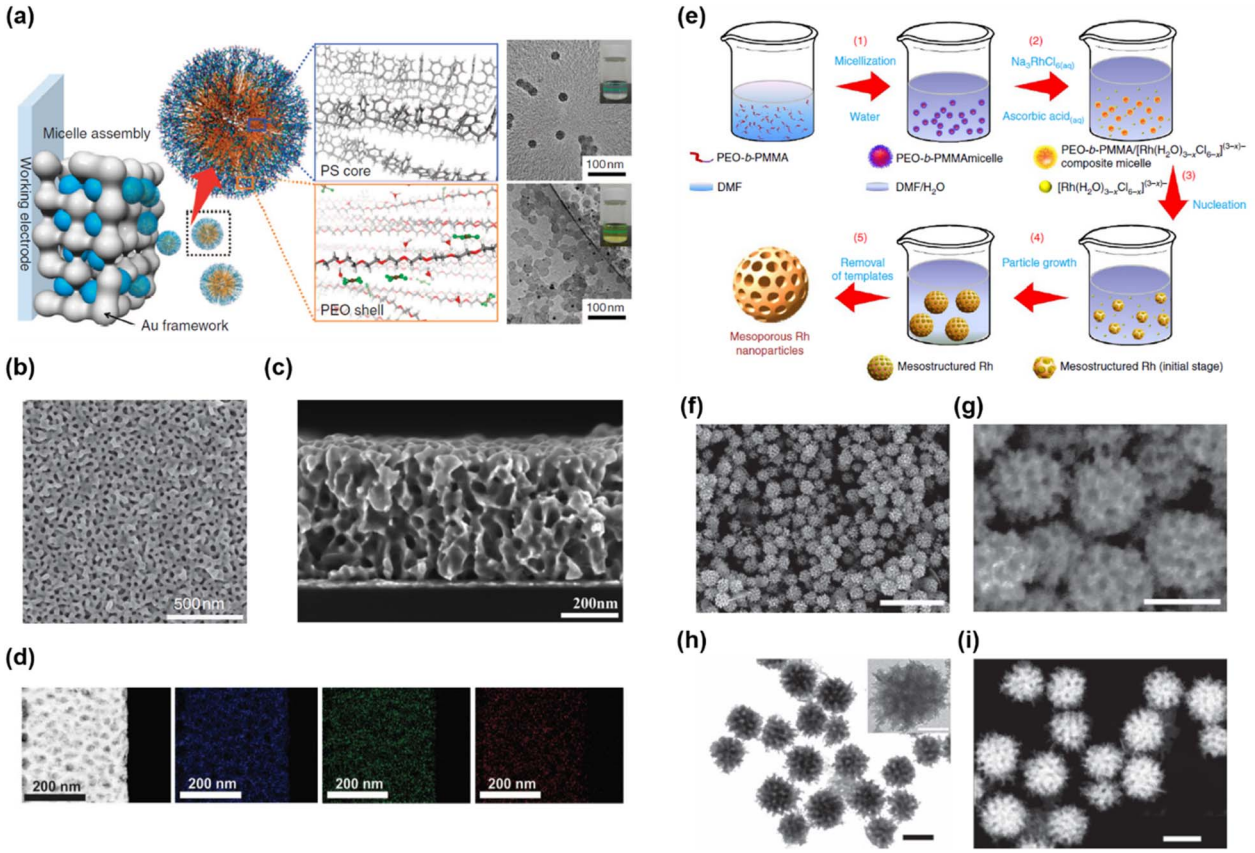

Fig. 9 (a) Synthetic concept of mesoporous Au films. (b and c) Top and cross-sectional SEM images of mesoporous Au films. (d) STEM image and EDS elemental mapping of the mesoporous AuCuNi film.[194] Copyright 2015, Nature Publishing Group. (e) Formation mechanism for mesoporous Rh nanostructures. (f and g) SEM images of mesoporous Rh nanoparticles. (h) TEM and (i) STEM images of mesoporous Rh nanoparticles.[195] Copyright 2017, Nature Publishing Group.

spherical micelles of PS-*b*-PEO on a conductive substrate. Then, electrochemical deposition was conducted by applying a potential to the substrate in an aqueous solution of $HAuCl_4$. The hydrophilic PEO blocks in the PS-*b*-PEO films could interact with the Au precursor in an aqueous solution. As electrochemical deposition progressed, the mesostructured composite of PS-*b*-PEO and Au started from the bottom of the PS-*b*-PEO film. Mesoporous Au films were obtained after template removal using an oxygen plasma (Fig. 9b and c). Mesoporous Au films of various thicknesses and pore sizes were synthesized by adjusting the electrochemical deposition time and volume fraction (or length) of the PS block in PS-*b*-PEO. Moreover, this synthetic method was extended to various metals (Cu,[196] Pd,[197] Ni,[198] Pt,[199] and Rh[195]) and metal alloys (Pt–Pd,[197,200] Pt–Cu,[201] and AuCuNi) (Fig. 9d).[43] They also reported a synthetic approach for mesoporous metal NPs using wet chemical synthesis (Fig. 9e).[195] To synthesize mesoporous Rh, PEO-*b*-poly(methyl methacrylate) copolymer (PEO-*b*-PMMA), Na_3RhCl_6, and ascorbic acid (AA) were used as the SDA, metal precursor, and reducing agent, respectively. Mesostructured composites were successfully prepared after chemical reduction by assembling the above three compounds in DMF/H_2O mixed solvents. After consecutive washing with an appropriate solvent, mesoporous Rh nanoparticles were obtained (Fig. 9f–i).

3.4. Metal nitrides

Metal nitrides have been extensively investigated because of their high electrical conductivity, outstanding thermal and electrochemical stability, and corrosion resistance.[192] The synthesis of mesoporous metal nitrides can maximize the surface area and mass transfer, thereby improving their performance in various applications such as energy storage, energy conversion, catalysis, and sensors.[202–205]

Because the synthesis of most metal nitrides involves a high-temperature nitridation process, the hard-template method has been used to maintain their mesoporous structure. Although hard template-based synthesis can produce high-quality mesoporous metal nitrides, this approach has disadvantages of long processing time and high cost. Thus, soft-template-based synthesis is preferred for synthesizing a wide range of mesoporous metal nitrides. However, nitridation without structural collapse remains a challenge because the template cannot be maintained during high-temperature nitridation.

To solve this problem, Ramasamy *et al.* introduced a carbon-supported synthetic approach using a block copolymer as a soft template.[37] A mesostructured composite was prepared by co-assembling F127, $TiCl_4$, and resol. After calcination at 700 °C under a nitrogen flow, a mesoporous TiO_2–C composite was obtained. Mesoporous TiN–C was synthesized after nitridation at

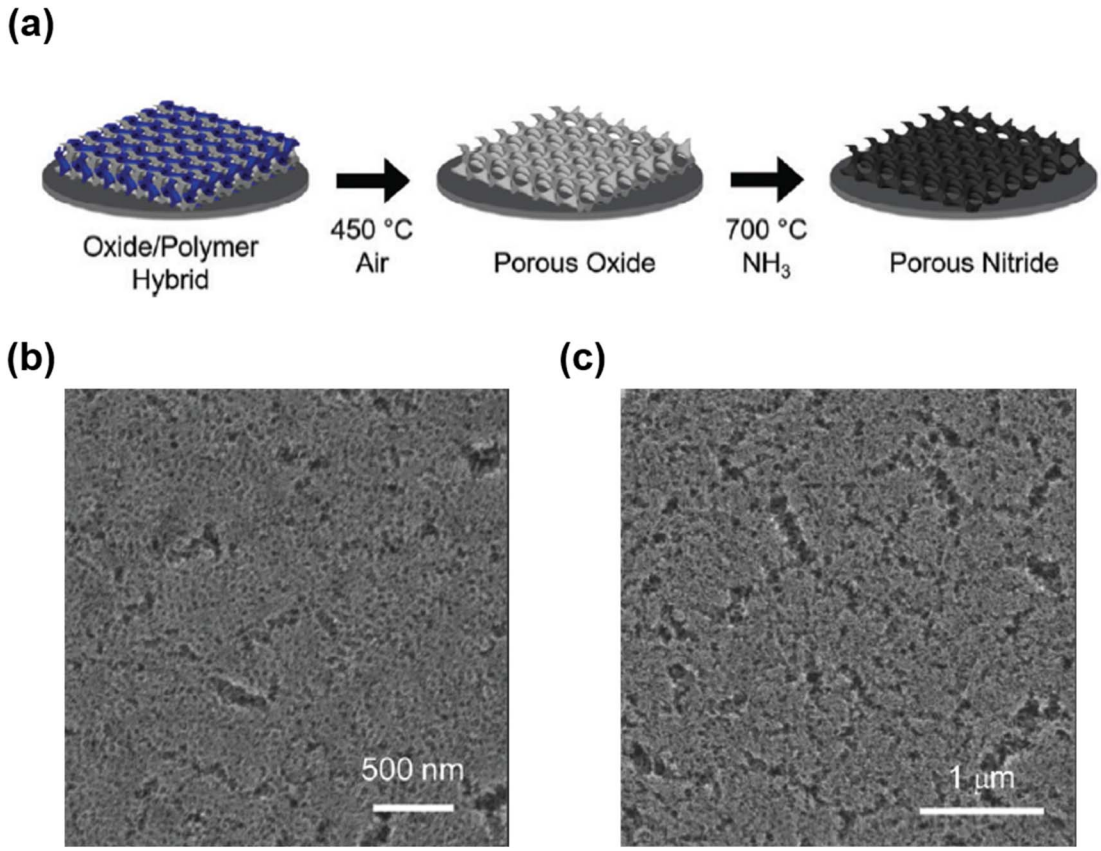

Fig. 10 (a) Schematic of the two-step heat treatment used to convert a mesostructured composite to a mesoporous metal nitride thin film. In the first step, an air heat treatment is used to form a mesoporous metal oxide thin film, which is converted to a porous nitride film in the second step by heating under NH_3. SEM images of (b) porous NbN and (c) TiN.[206] Copyright 2017, Royal Society of Chemistry.

700 °C, suggesting that TiO_2 in TiO_2–C was successfully converted to TiN without structural collapse. The amorphous carbon in TiO_2–C prevented the aggregation and growth of TiN crystals during nitridation. Although successful nitridation was possible while maintaining the mesoporous structure, the pore size was relatively small (8 nm) because of the low molecular weight of F127. Meanwhile, when a high-molecular-weight BCP is used as the SDA, mesoporous nitride with a large pore size can be obtained.[37] For example, Fritz *et al.* recently synthesized mesoporous TiN and NbN using a PI-*b*-PS-*b*-PEO copolymer (ISO) as the SDA (Fig. 10a).[206] Calcination was performed to remove ISO at 450 °C after preparing a mesostructured composite through the co-assembly of ISO and metal oxide precursors. During calcination, ISO was decomposed, leading to the formation of mesoporous Nb_2O_5 and TiO_2 and subsequent conversion to mesoporous NbN and TiN after nitridation at 700 °C under an NH_3 flow (Fig. 10b and c).

4. Innovative soft-template synthesis for various hierarchical morphologies of mesoporous materials

4.1. Hierarchically structured mesoporous materials

Materials with hierarchical pores have synergetic benefits originating from different pore size regimes, such as highly improved mass transport through macropores and high specific surface area due to the presence of micropores and mesopores.[207] Thus, hierarchical porous materials can be used for high-performance energy storage, energy conversion, catalysis, and sensors.[208–211]

Hierarchical porous materials are synthesized by using a multiple templating method that combines hard and soft templates.[212] Fig. 11 shows a scheme of multiple-template synthetic methods. Although hierarchical porous materials with various macroporous structures are synthesized using hard (such as AAO, silica, colloidal crystals, and metal oxides)[213,214] and soft templates (small molecule surfactants and BCPs), such synthetic routes require complicated time-consuming processes.

Sai *et al.* successfully fabricated a hierarchical porous scaffold consisting of mesopores and macropores by using only a soft-templating method.[215] They dissolved an appropriate amount of PS-*b*-PEO and oligomer PEO in xylene and then induced solvent evaporation at 130 °C. During solvent evaporation, spinodal decomposition (SD) of PS-*b*-PEO and oligomer PEO and microphase separation of PS-*b*-PEO occurred. After the selective removal of the oligomer PEO by rinsing with water, they obtained a macroporous polymeric wall composed of cylindrical mesopores. Although hierarchically structured organic materials were fabricated using this approach, the

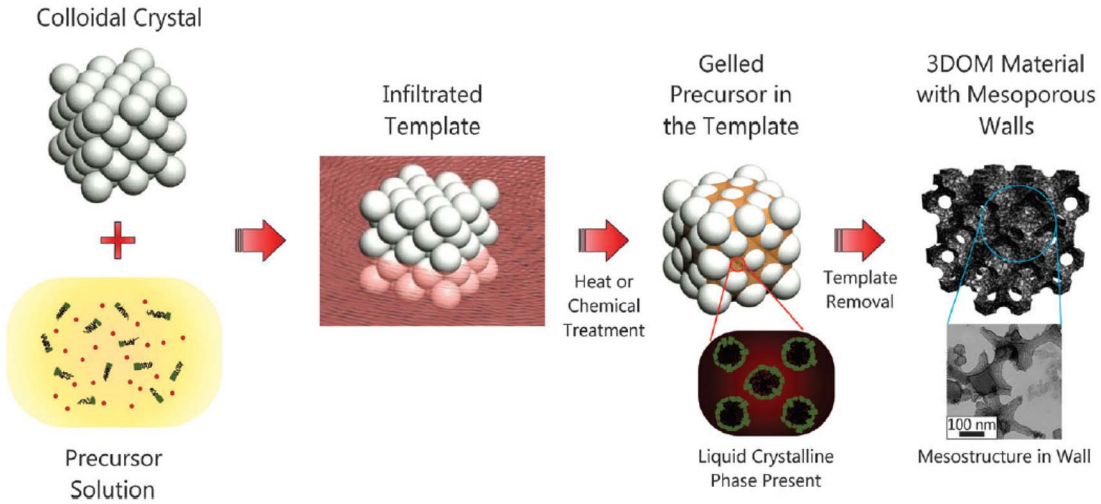

Fig. 11 Schematic of a multiple templating approach.[212] Copyright 2013, Royal Society of Chemistry.

hierarchical structure of inorganic materials was difficult to control because of the difficulty in simultaneously controlling both the sol–gel reaction of inorganic precursors and macro-/meso-phase separation behavior.

Lee's group reported a versatile method for synthesizing hierarchically porous inorganic materials.[216] They employed PS-*b*-PEO as a soft template, phenol–formaldehyde resin (resol) as an additive to induce macrophase separation, and tetraethyl

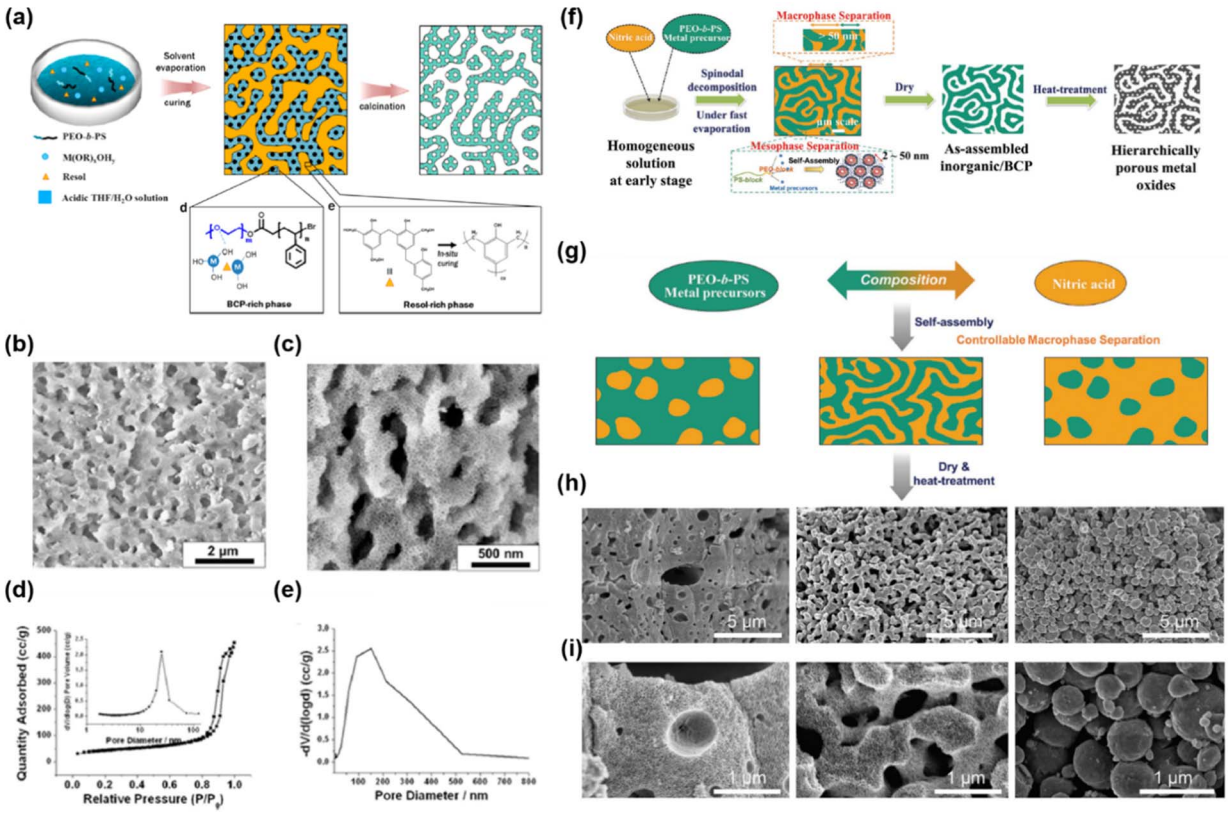

Fig. 12 (a) Schematic of the hierarchical assembly of micro and macrophase separation. (b and c) SEM images of h-SiO_2 on different length scales. (d) N_2 physisorption isotherm and (inset) mesopore size distribution. (e) Macropore size distribution determined by mercury intrusion porosimetry.[216] Copyright 2014, American Chemical Society. (f) Schematic of multiscale phase separation for the synthesis of hierarchically macro and mesoporous metal oxides. (g) Schematic of macrophase separation controlled by different ratios of acid phase to precursor/PS-*b*-PEO phase. (h and i) SEM images of various hierarchical porous structures obtained from multiple phase separation.[207] Copyright 2018, Wiley-VCH.

orthosilicate (TEOS) as a silica source (Fig. 12a).[216] During evaporation of the solvent from the solution, a resol-rich phase and a (resol/silicate/PS-*b*-PEO)-rich phase were formed through macrophase separation. In the (resol/silicate/PS-*b*-PEO)-rich phase, silicate and resol were incorporated into the PEO microdomains and thus formed an ordered mesostructure by microphase separation. Thermopolymerization (curing) of the resol in the resol-rich phase supports the overall framework. After calcination to remove the PS-*b*-PEO and cured resol, three-dimensionally interconnected meso/macroporous silica was obtained. The hierarchical porous structure exhibited mesopores with, a dominant pore size of 25 nm and a narrow size distribution (Fig. 12d), as well as macropores with diameters ranging from 50 nm to 400 nm (Fig. 12e). In addition, they synthesized hierarchically porous TiO_2 and Nb_2O_5.[217] Recently, they proposed another method to synthesize hierarchical porous structures using evaporation-induced SD (Fig. 12f).[207] Multiple-phase separation was induced by controlling the evaporation conditions of THF and nitric acid in a mixed solution containing PS-*b*-PEO/precursors/THF/nitric acid. The selective evaporation of THF resulted in macrophase separation of the PS-*b*-PEO/precursors phase and nitric acid. Simultaneously, microphase separation of PS-*b*-PEO occurred, resulting in the formation of a hierarchical macro/mesostructured composite. After calcination, the composite was converted to hierarchical porous metal oxides. They also synthesized various hierarchical porous materials including SiO_2, carbon, WO_3, TiO_2, and titanium–niobium oxides. In addition, they reported that macrophase separation could depend on the composition ratio of nitric acid to the PS-*b*-PEO/precursor phases (Fig. 12g), resulting in various macrostructures such as mesoporous structures containing isolated macropores, co-continuous macro/mesoporous structures, and spherical mesoporous structures (Fig. 12h–i).

4.2. Mesoporous materials with confined morphologies

Confining the mesoporous structure to a macroscopic shaped cavity can enhance physiochemical properties that cannot be improved by conventional mesoporous materials.[218] For example, synergistic effects can be obtained by combining high surface area, large pore volume, and enhanced mass/ion accessibility originating from the mesoporous structure with the advantage of macroscopic morphologies.[219–221] To synthesize confined morphologies of mesoporous materials, Lee's group reported various strategies based on SD and soft-templating methods.[103,145,222] They designed prehydrolyzed aluminosilicate (AS)/PS-*b*-PEO/homo PS or PMMA blend systems (Fig. 13a and b).[103] When the solvent evaporates from the blend solution, macrophase separation of homopolymers and AS/PS-*b*-PEO phases and the microphase separation of PS-*b*-PEO occur, creating a confined structure with a mesostructured sphere in

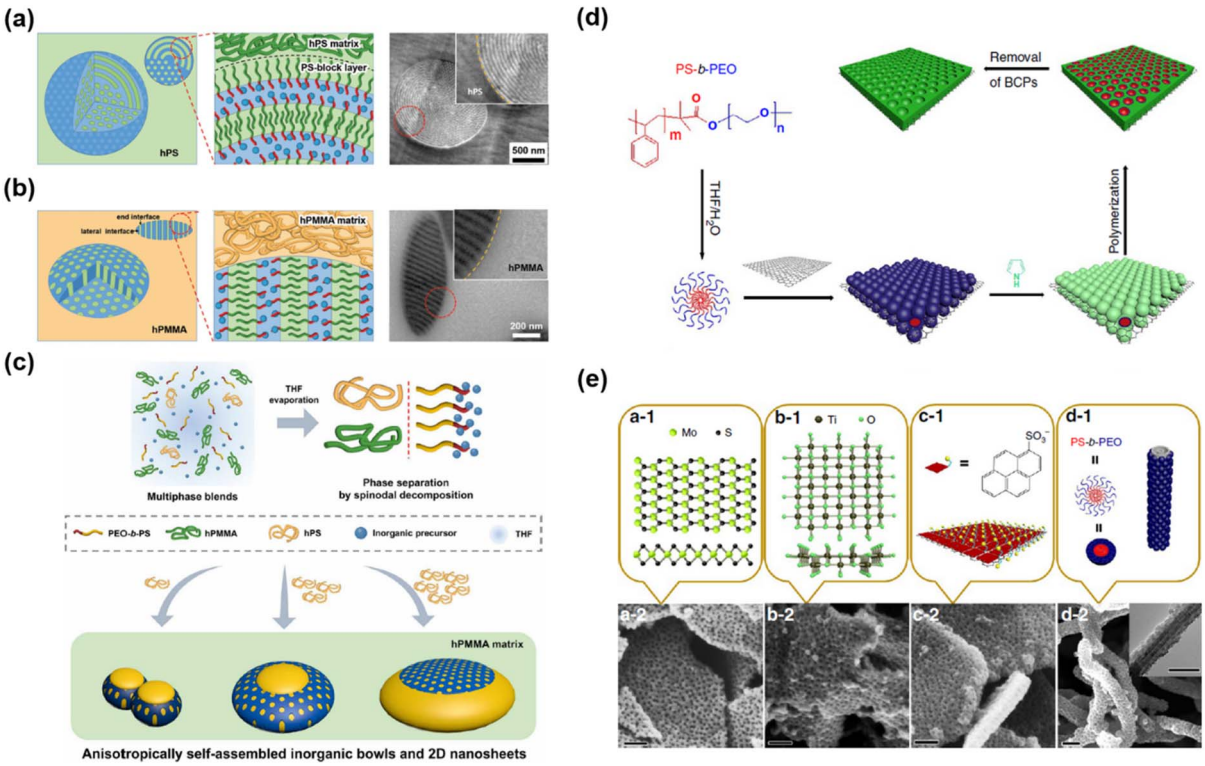

Fig. 13 Effect of the homopolymer matrix on the pore orientation and shape of inorganic particles prepared in (a) PS and (b) PMMA homopolymers.[103] Copyright 2018, Wiley-VCH. (c) Schematic of the preparation of bowl-like inorganic particles and 2D mesoporous nanosheets.[222] Copyright 2020, The American Association for the Advancement of Science. (d) Patterning of 2D surfaces with mesoporous conducting polymer nanosheets. (e) Patterning of various functional free-standing surfaces, including MoS_2, titania, exfoliated graphene, and CNTs.[223] Copyright 2015, Nature Publishing Group.

the homopolymer matrix. Here, the pore orientation and particle shape were adjusted by changing the homopolymer type. For the PS homopolymer, owing to the preferential interaction between the PS block of PS-*b*-PEO and the PS matrix, the AS/PS-*b*-PEO phase showed a parallel orientation of the cylindrical microdomain to the interface (Fig. 13a). Meanwhile, for the PMMA homopolymer, because PMMA homopolymers are enthalpically neutral favorable for both PEO/precursors and PS blocks, the AS/PS-*b*-PEO phase exhibited a perpendicular orientation of the cylindrical microdomain to the interface of the PMMA matrix. Furthermore, they implemented a higher level of multiscale structure by mixing homo PS and homo PMMA binary blends and AS/PS-*b*-PEO. Here, PS-*b*-PEO acted as both a compatibilizer and SDA. In PS-*b*-PEO, the PS block is compatible with homo-PS, whereas the PEO block is more compatible with homo-PMMA. Consequently, the mesostructured AS/PS-*b*-PEO could be located at the interface between PMMA and PS to minimize the PS/PMMA interfacial contact area.

Using ternary-polymer blend systems, they also synthesized mesostructured materials confined in bowls and 2D nanosheets (Fig. 13c).[145,222] To fabricate confined mesoporous materials, they used PS-*b*-PEO as the SDA, excess homo PMMA as the organic matrix, homo PS as one of the minor components, and AS as an inorganic precursor. During solvent evaporation from the solution containing the above components, macrophase separation of the homo PS, homo PMMA, and PS-*b*-PEO/AS phases occurred, resulting in dispersed homo PS and PS-*b*-PEO/AS phases in the homo PMMA matrix. PS-*b*-PEO is immiscible with both high-molecular-weight homo PS and homo PMMA, while homo PS and homo PMMA are immiscible with each other. Therefore, macrophase separation occurred because of the immiscibility of the three phases. The PS-*b*-PEO/AS and homo PS phases were in contact with each other to reduce the interfacial tension and existed in dispersed phases in the homo PMMA matrix. Owing to the compatibility of the PS block of PS-*b*-PEO with homo PS, the surface of the PS-*b*-PEO/AS phase was partially covered with homo PS. In addition, because the homo PMMA matrix is neutral to both PS and PEO/AS of the PS-*b*-PEO/AS phase, the microdomains of PS-*b*-PEO/AS were oriented perpendicular to the interface of the PMMA matrix. Therefore, the confined mesoporous AS particles obtained after calcination consisted of highly accessible, open cylindrical pores. Furthermore, by changing the relative molecular weight of homo PS with respect to that of PS-*b*-PEO ($r_M = M_{hPS}/M_{BCP}$), various confined shapes were obtained. For example, in the range of $0.2 \leq r_M \leq 2$, the size of particles and concavities increased as r_M increased, maintaining mesopore sizes. At a high r_M value, the PS-*b*-PEO/AS rich phase became extremely thin with monolayered micelles, resulting in mesoporous inorganic nanosheets. Various compositions comprising carbon, TiO_2, and Nb_2O_5/C have also been synthesized.[139,145,217]

Liu *et al.* demonstrated a universal strategy for synthesizing confined mesoporous conducting polymers with 2D morphology by inducing the orientation of SDAs and monomers on the surface of 2D nanosheets (Fig. 13d).[223] First, PS-*b*-PEO (SDA) forms spherical micelles in a mixture of THF and H_2O, which are organized on the 2D surface of graphene oxide through hydrogen bonding. The formed micelles serve as guides for the polymerization of the conducting polymer monomer (pyrrole or aniline). After the removal of SDAs, mesoporous conducting polymers (polypyrrole (PPy) and polyaniline (PANi)) confined to the 2D surfaces of graphene oxide were obtained. This approach can be applied to various functional surfaces, including 2D exfoliated graphene (EG), MoS_2, titania nanosheets, and 1D carbon nanotubes (CNTs), yielding confined mesoporous materials with various functional surfaces.

4.3. User-customized mesoporous materials

To date, soft-templating methods have been mainly investigated for the synthesis of mesoporous materials in bulk. However, to expand the application of mesoporous materials to microelectronics or mobile devices, the production of materials with various customized shapes, including thin films, patterned shapes, and complex 3D architectures are preferable.

Tan *et al.* demonstrated a simple pattern of mesoporous thin films by combining soft templating and laser-induced transient heating (Fig. 14a).[33] They used PI-*b*-PS-*b*-PEO or Pluronic F127 as the SDA and oligomeric resols as precursors. PI-*b*-PS-*b*-PEO and resols were first dissolved in a solvent and spin-coated on a boron-doped silicon substrate to form a mesostructured hybrid thin film, which was subsequently irradiated with a continuous-wave CO_2 laser. During laser irradiation, the boron-doped Si substrate absorbed most of the laser energy and dissipated heat, leading to simultaneous thermopolymerization of the resol and decomposition of BCP. Therefore, the mesoporous carbon thin film remained in the laser-passed region. After the nonirradiated region was selectively rinsed, a patterned mesoporous carbon thin film was obtained (Fig. 14b). Additionally, various pore sizes were implemented by tailoring the mass ratio of resol and the SDA, as well as the molecular structure of the SDA. Yu *et al.* fabricated patterned mesoporous thin films by combining photolithography and soft templating (Fig. 14c).[110] They prepared a mesostructured composite comprising PI-*b*-PS-*b*-PEO and niobium oxide precursor thin films by spin-coating. The as-made composite films were then readily patterned through a conventional photolithography process. After etching and photoresist removal, a mesoporous thin film with a well-defined pattern was obtained (Fig. 14d and e). However, this method requires multiple processes, including selective rinsing and conventional photolithography. In contrast, printing technology that directly deposits a solution on a desired region of a substrate can easily provide a patterned thin film without multiple processes. Soft-templating methods are based on solution-phase synthesis and are relatively easy to combine with printing technology. However, to prevent nozzle clogging during printing, the evaporation rate of the solvent and reactivity of the precursors should be carefully controlled. Devabharathi *et al.* recently fabricated mesoporous metal oxides in a selective area using inkjet printing.[224] They prepared a homogeneous ink by mixing Pluronic F-127 as the

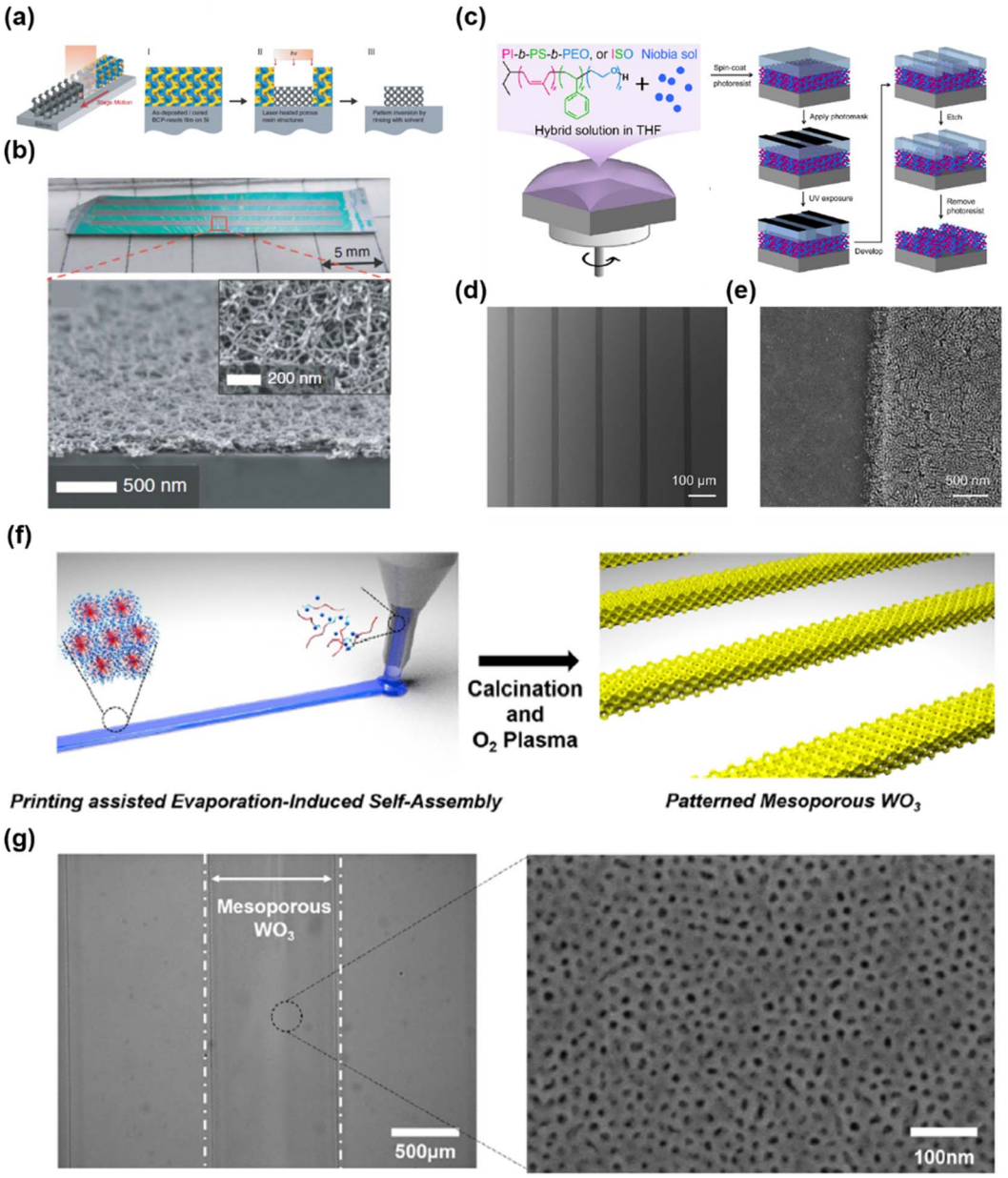

Fig. 14 (a) Schematic of the transient laser heating process for synthesizing patterned mesoporous carbon. (b) Optical image and cross sectional and plane SEM images (inset) of macroscopic trenches after CO_2 laser irradiations.[33] Copyright 2015, The American Association for the Advancement of Science. (c) Schematic of the combination of photolithography and soft templating. (d and e) SEM images of a patterned niobium carbonitride thin film.[110] Copyright 2021, American Chemical Society. (f) Schematic illustration of printing-assisted evaporation-induced self-assembly. (g) OM (left) and SEM (right) images of a patterned mesoporous WO_3 film.[13] Copyright 2020, Nature Publishing Group.

SDA and metal chloride precursors with an appropriate solvent. During printing, the solvent evaporated and co-assembly of F-127 and the precursors occurred, resulting in a mesostructured composite film. Subsequently, a mesoporous metal-oxide film was obtained after calcination. Moreover, they synthesized various mesoporous metal oxides, including In_2O_3, ITO, CuO, and SnO_2. Inkjet printing is based on drop-on-demand; therefore, this approach is not suitable for large-scale and continuous line production. By contrast, extrusion-based printing is more suitable for covering a large area or a large amount of material because of continuous ink ejection.

Kim *et al.* demonstrated that mesoporous WO_3 was successfully patterned over a large area by combining the EISA protocol with electrostatic-force-assisted dispensing printing (Fig. 14f).[13] They mixed PS-*b*-PEO as a SDA and WCl_6 as a precursor in a mixture of tetrahydrofuran and ethanol. When the obtained solution was printed on fluorine-doped tin oxide (FTO)-coated glass, co-assembly of PS-*b*-PEO and WCl_6 occurred as the solvent evaporated, resulting in a mesostructured

composite. Patterned mesoporous WO_3 was then formed after template removal through calcination and oxygen plasma treatment (Fig. 14g). As the sample stage was controlled by using a computer, user-customized patterning was easily achieved over a large area (10 cm^2). In addition to the synthesis of patterned mesoporous thin films, achieving the desired shape of mesoporous materials in three dimensions can extend their applications. In particular, the synthesis of 3D geometry architecture consisting of interconnected mesopores is important for biomedical applications such as bone regeneration[226] and drug delivery.[227,228] Several groups have attempted to synthesize 3D structured mesoporous materials using 3D printing but failed to achieve high surface area and complex geometry.[229–231] Recently, Shukrun Farrell *et al.* introduced a method for synthesizing mesoporous silica with complex 3D geometry.[225] They integrated a soft-templating method with digital light processing, which is a stereolithography 3D printing technology that applies patterned UV light to cure sequential 2D layers of UV-polymerizable ink to create 3D objects. First, TEOS was added to a solution containing Pluronic F-127. At this time, hydrolysis and condensation of TEOS occurred near F-127 micelles, and mesoporous silica skeletons were thus formed. Next, UV-curable ink containing an epoxy aliphatic acrylate as a monofunctional monomer, aliphatic urethane diacrylate as a cross-linker, and a photoinitiator was added to the above solution to enable photopolymerization. During UV irradiation, photopolymerization occurred to form a user-customized shape, resulting in an elastomer containing mesostructured silica. Finally, after high-temperature calcination, the elastomer and organic template decomposed, leaving pure silica. The synthesis of mesoporous materials in user-customized shapes (selective area or desired architecture) is expected to not only save production costs but also expand the existing standardized shapes of ESSs in the future.

5. Application of mesoporous materials to energy storage systems

Mesoporous materials prepared by the soft-templating method confer considerable advantages to ESSs owing to their high surface area, large pore volume, tunable pore size, and shape.[232] The high surface area provides abundant active sites by maximizing the interface between the electrolyte and active materials.[233] In addition, the large pore volume provides the accommodation of volume expansion and strain relaxation of materials during the repeated charge/discharge of ESSs.[142] Device performance can be maximized by tailoring the pore size and shape of mesoporous materials to meet the needs of various ESSs. Although many research groups have successfully enhanced the performance of ESSs by synthesizing various mesoporous materials, we only focused on batteries and supercapacitors based on mesoporous materials.[105,234,235]

5.1. Batteries

Increasing energy requirements necessitate the development of ESSs for sustainable energy supply. For such a purpose, rechargeable batteries are believed to be the most feasible option among various ESSs because of their long cycle life, high energy efficiency, and simple maintenance. Diverse rechargeable batteries with different charge carriers such as Li^+, Na^+, K^+, Ca^{2+}, Mg^{2+}, Zn^{2+} and Al^{3+} have been demonstrated.[236–242] Numerous research studies on various mesoporous cathode[142,243–251] and anode[55,145,155,252–260] materials have been reported to improve the energy storage performance of batteries.

Graphite is the most popular anode material for lithium-ion batteries (LIBs) owing to its low cost, excellent electrical conductivity, and high chemical stability. However, the development of LIBs with high energy density is hampered by the low capacity of graphite (372 mA h g^{-1}). Thus, ordered mesoporous carbons (OMCs) have attracted considerable attention as alternatives to graphite because of their high specific surface area and large pore volume, providing numerous active sites for Li^+ adsorption and storage.[234,235] Velez *et al.* synthesized mesoporous carbon materials and compared them with graphite when applied as anodes for LIBs.[34] The synthesized mesoporous carbon consisted of mesopores (~7 nm) and exhibited large surface area (769 m^2 g^{-1}) and pore volume (1.4 cm^3 g^{-1}). These characteristics provided abundant mesopores for storing large amounts of Li ions, resulting in notable electrochemical properties as an anode material for LIBs with a high capacity (670 mA h g^{-1}) exceeding that of graphite (358 mA h g^{-1}). In addition, the pore size and wall thickness of the mesoporous carbon play a major role in determining energy storage performance. Mesoporous metal oxides have been developed as anode materials in alkaline-ion battery systems because of their high theoretical capacities.[261] For example, Ti-based oxides are particularly interesting because they prevent the formation of solid electrolyte interface (SEI) layers and guarantee structural stability. Furthermore, Ti is an abundant element, thus making it a cost-effective material.[154] For the first time, Kang *et al.* synthesized a mesoporous $Li_4Ti_5O_{12}$ (LTO)–carbon nanocomposite (Meso-LTO–C) and reported its excellent performance as an anode material in LIB systems.[154] The synthesized mesoporous LTO consisted of mesopores (~20 nm) and exhibited a large pore volume (0.148 cm^3 g^{-1}) and surface area (68.7 m^2 g^{-1}). When Meso-LTO–C and bulk-LTO were applied as anode materials for LIBs, Meso-LTO–C exhibited a superior electrochemical performance with a capacity of 115 mA h g^{-1} at a 10C rate compared to a bulk-LTO LIB because of its large surface area and easy ion accessibility. Despite the high stability and rate capability of Ti-based oxides, the theoretically low lithium charge capacity (<200 mA h g^{-1}) and loss of energy density from the relatively high Li^+ insertion voltage (>1.5 *vs.* Li/Li^+) remain limitations to the use of anodes with a Ti^{4+}/Ti^{3+} redox couple. Titanium–niobium oxides have been introduced as alternative anode materials because of their high lithium charge capacity and broad lithium charge potential (1.7–1.0 V).[155] Guo *et al.* synthesized mesoporous $TiNb_2O_7$ and demonstrated its successful application as a high-capacity anode in LIBs.[262] The large mesopores (~22 nm) and high surface area (48 m^2 g^{-1}) of the mesoporous TNO (m-TNO) electrode yielded a high reversible capacity (281 mA h g^{-1}) that was almost twice

that of LTO (~160 mA h g^{-1}). In addition, the performance of the m-TNO electrode was markedly superior to those of reported Ti- and Nb-based electrodes.[262]

The simultaneous integration of multiscale porous structures can produce synergistic properties. For example, the combination of macropores and mesopores can benefit from the effective mass transport from macropores and abundant reaction sites from mesopores. Recently, Jo *et al.* demonstrated a high-performance LIB by applying hierarchically structured anode materials.[207] They synthesized co-continuous macro/mesoporous titanium–niobium oxides (ccm-TNO) and then compared the LIB electrode performance of the ccm-TNO with m-TNO without macropores. Although the two electrode materials had similar structural properties (surface area, pore volume, pore size, and crystal size), their electrochemical performances showed significant differences. For example, at a rate of 0.2C, ccm-TNO exhibited a higher capacity (257 mA h g^{-1}) than m-TNO (215 mA h g^{-1}). Additionally, the cmm-TNO electrode retained 44% of its maximal capacity (112 mA h g^{-1}) at 60C rate, whereas the m-TNO electrode only retained 33% of its capacity. These results indicate that the introduction of macropores into the mesoporous structure could improve electrochemical performance by providing enhanced ionic transport compared with the mesoporous structure alone.

Mesoporous structures provide high surface area and fast ion transport, but stable loading of host materials is restricted due to their small pore size. In contrast, macroporous structures have a relatively small surface area, but their large pore volume allows a large amount of host material loading. Therefore, these two advantages can be synergistically combined by introducing macropores into the mesoporous structure. Lim *et al.* applied these advantages to a lithium–sulfur battery (LSB) system (Fig. 15a and b).[105] LSBs have been recognized as an alternative to LIBs because of their high theoretical energy density (2600 W h kg^{-1}), but their practical use is limited by their low conductivity and the sluggish redox kinetics of sulfur. To solve these problems, stable loading of sulfur into the porous material is crucial, requiring careful control of the porous architecture to improve the performance of LSBs. Co-continuous hierarchical macro/mesoporous titanium nitride (h-TiN) was synthesized as a sulfur host. The obtained h-TiN consisted of mesopores (32 nm) and had a surface area and pore volume of 47 m^2 g^{-1} and 0.3 cm^3 g^{-1}, respectively. To evaluate the effect of macropores on LSB performance, they also prepared mesoporous TiN (m-TiN) with virtually identical structural properties (pore size, pore volume, and surface area). When the same amount of sulfur (~72 wt%) was impregnated into both TiN samples, h-TiN was stably filled without the growth of sulfur particles; by contrast, m-TiN showed sulfur particles aggregated on the surface of the mesopores (Fig. 15a). This aggregation was due to the large space of macropores, which provided sufficient space for sulfur loading. The initial discharge and charge capacities of h-TiN were 1040 and 1037 mA h g^{-1}, respectively, which were higher than those of m-TiN (739 and 741 mA h g^{-1}, respectively). In addition, h-TiN showed superior electrochemical performance at a high rate of 5C compared to m-TiN (Fig. 15b) because sulfur was stably loaded in the interconnected macropores.

Miniaturization of ESSs enables efficient usage of space and maximizes volumetric or areal energy storage performance,

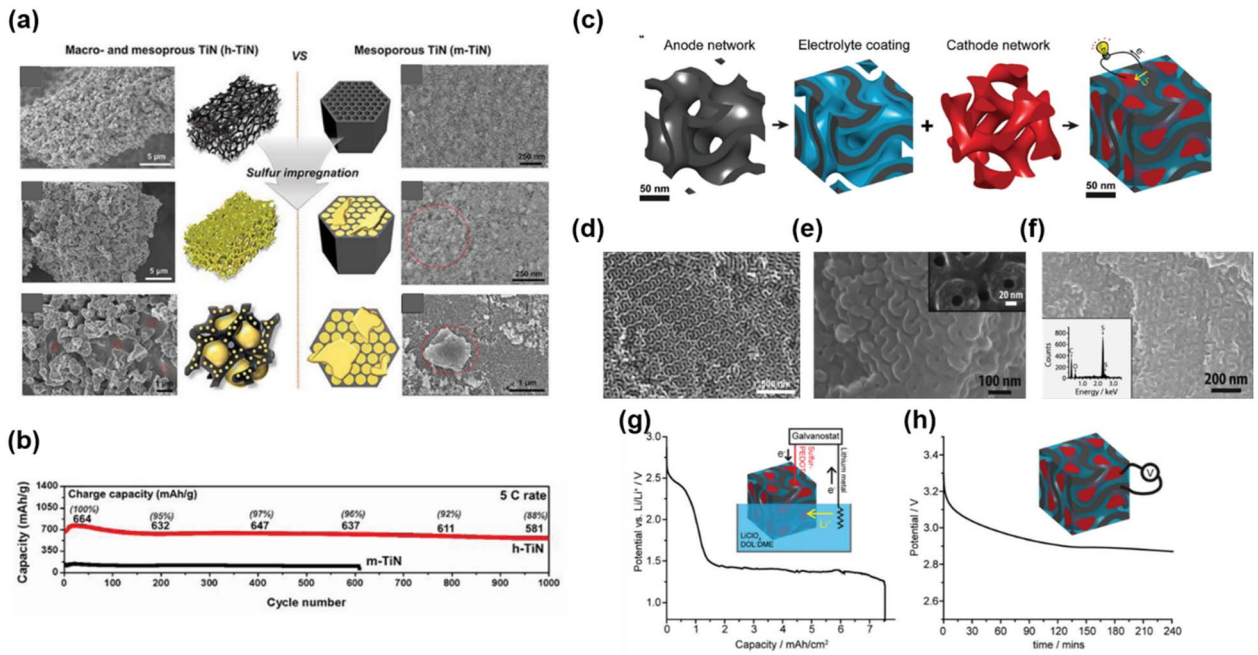

Fig. 15 (a) SEM images of h-TiN and m-TiN before and after sulfur impregnation. (b) The galvanostatic test of h-TiN and m-TiN at a high current density of 5C rate.[105] Copyright 2019, Wiley-VCH. (c) Schematic of the synthetic pathway. SEM images of (d) G^DMC, (e) PPO-coated G^DMC, and (f) gyroidal nanohybrid. (g) Potential during external lithiation of the gyroidal sulfur–PEDOT phase *vs.* lithium metal in liquid electrolyte. (h) Open-circuit voltage of the solid-state gyroidal hybrid over the first 4 h after charge.[142] Copyright 2018, Royal Society of Chemistry.

providing many opportunities for integration with other electronic devices. Conventional planar 2D stacked configurations of ESSs entail a waste of space on a macroscopic scale. For example, the electrolyte/separator layer between the anode and cathode occupies a micrometer-scale space. The fabrication of a bicontinuous anode–electrolyte–cathode layer at the nanometer scale can solve this issue. Although this concept has already been established,[142] its implementation has been

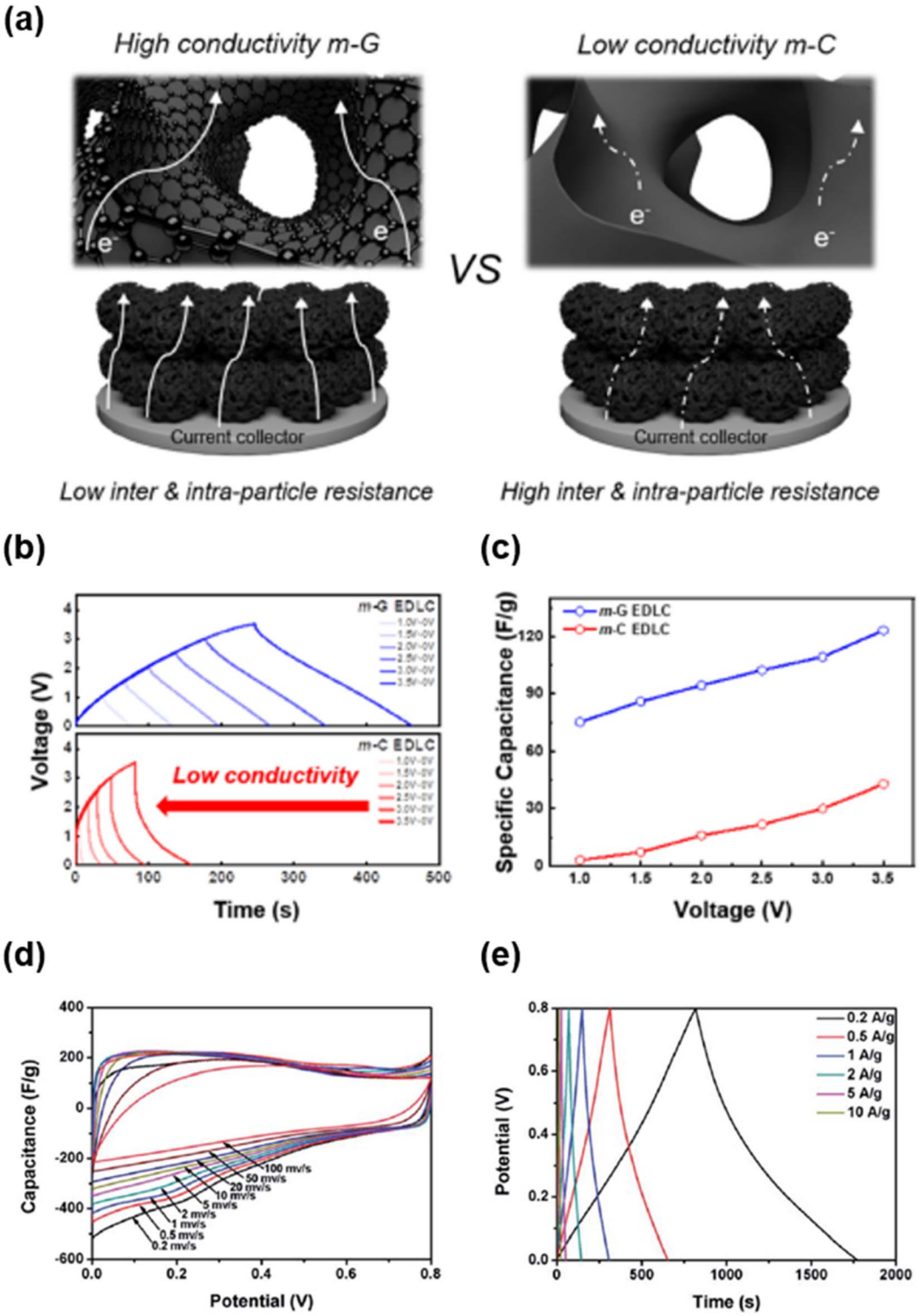

Fig. 16 (a) Schematic of electron transport in m-G (left) and m-C (right) EDLCs. (b) Galvanostatic charge/discharge curves of EDLCs at various operation voltages up to 3.5 V. (c) Specific capacitance of EDLCs at various operation voltages.[233] Copyright 2022, American Chemical Society. (d) CV curves and (e) galvanostatic charge/discharge curves of the N-doped mesoporous carbon.[28] Copyright 2018, Royal Society of Chemistry.

difficult because of strict material requirements and the complexity of their nanofabrication. Recently, Werner *et al.* successfully fabricated a cathode–electrolyte–anode system with a 3D bicontinuous network with a size less than 50 nm and demonstrated its battery operation (Fig. 16c–h).[142] First, they synthesized gyroidal mesoporous carbon (G^DMC) monoliths that satisfied certain prerequisites (lithium redox, electrical conductivity, and structural integrity) to act as anodes and provided sufficient space for nanoconfinement of the electrolyte and cathode layers. Subsequently, a thin film of poly(phenylene oxide) (PPO) (thickness of less than 10 nm) was uniformly coated on the surface of the G^DMC monoliths by electropolymerization. This PPO thin film allowed ionic transport while ensuring electronic insulation between the anode and cathode layers. Finally, bifunctional sulfur–poly(3,4-ethylenedioxythiophene) (PEDOT) was filled into PPO-coated G^DMC through an *in situ* infiltration–polymerization method. Here, sulfur and PEDOT were selected as the redox-active material and current collector, respectively. To introduce lithium, the sulfur–PEDOT phase was electrochemically reduced using lithium metal as the counter electrode (Fig. 15g). After charging to 3.5 V, the gyroidal nanohybrid exhibited a stable open-circuit voltage of 2.8 V for several hours (Fig. 15h). In addition, a well-defined discharge plateau was maintained for 20 cycles. Nanoscale 3D bi-continuous network ESSs are in an early state of research but they would provide help to fabricate a new type of battery in the future.

5.2. Supercapacitors

Compared to batteries, supercapacitors (SCs) exhibit higher power densities, superior long-term stability, and higher rate capabilities.[263–266] Therefore, they are mainly used for applications that require high power density and long lifetimes that cannot be achieved by batteries. The energy storage mechanisms of SC materials can be divided into two categories: non-faradaic and faradaic reactions. In non-faradaic materials, energy is stored by forming an electric double-layer through physical adsorption and desorption of ions at the interface between electrolytes and active materials;[267–269] thus, these materials are mainly called electric double layer capacitors (EDLCs). Energy storage in EDLCs is fast and stable for a long time because it usually relies on the physical adsorption and desorption of ions.[270–272] Meanwhile, the energy storage mechanism of faradaic materials involves a redox reaction.[263,273] These materials exhibit inferior stability to non-faradaic materials but have high specific capacitance.

In an EDLC system, mesoporous carbon exhibits high capacitance and excellent rate capability. Graphitization of mesoporous carbon is another effective approach for improving the electrochemical performance of EDLCs by enhancing the electrical conductivity of active materials.[65,135] Kim *et al.* synthesized mesoporous graphene (m-G) and mesoporous carbon (m-C) with almost identical structures (pore size and surface area) to evaluate the effect of electrical conductivity (Fig. 16a–c).[233] Because interconnected graphene channels were distributed throughout its mesoporous structure, m-G exhibited lower inter/intra-particle resistance, thereby facilitating fast electron transport (Fig. 16a). With increasing operation voltage (0–3.5 V), the galvanic charging/discharging (GCD) curve of m-G maintained a symmetrical shape, whereas that of m-C was significantly distorted (Fig. 16b). In addition, at the highest operation voltage (3.5 V), the specific capacitance (123.3 F g^{-1}) of m-G was considerably higher than that (42.8 F g^{-1}) of m-C (Fig. 16c). These results imply that graphitization of a mesoporous carbon framework is an effective approach to significantly improve the electrochemical performance.

Heteroatom doping on the carbon surface is an effective strategy for enhancing the electrochemical performance by the addition of a pseudo-capacitive reaction. Many studies on doping mesoporous carbon with hetero atoms such as B, N, O, P, and S have been reported.[274–278] Liu *et al.* synthesized N-doped mesoporous carbon and prepared high-performance EDLCs (Fig. 16d and e).[29] The synthesized N-doped mesoporous carbon exhibited a high nitrogen content of 19 wt%, mesopores with pore sizes of 9.5–17.2 nm and large surface area (458–476 m^2 g^{-1}). The cyclic voltammetry (CV) curve of the N-doped mesoporous carbon showed a rectangular shape over the entire voltage range owing to the EDLC and reversible humps due to the faradaic reaction between 0.2 and 0.6 V (Fig. 16d). In addition, the symmetrical GCD curve indicated stable device operation (Fig. 16e). The specific capacitance was 225 F g^{-1} at 0.5 A g^{-1}, which was much higher than that of neat mesoporous carbon. These results are attributed to both the pseudocapacitive reaction of the nitrogen content and high surface area of the mesoporous structure. Many transition metal oxides exhibit pseudocapacitive behavior and have been widely utilized as pseudo-capacitor electrodes.[279–284] Kim *et al.* showed that a mesoporous tungsten trioxide (WO_3) film exhibited mesopores (~30 nm) and high specific surface area (32.14 m^2 g^{-1}).[13] At a current density of 0.02 mA cm^{-2}, the areal capacitances of a mesoporous WO_3 film were similar to that of a compact WO_3 film without mesopores. However, the mesoporous WO_3 film exhibited a much higher rate capability. The capacitance retentions of mesoporous and compact WO_3 were 68% and 34%, respectively, when the current density was changed from 0.02 mA cm^{-2} to 1.0 mA cm^{-2}. This difference is attributed to the effective and fast ion transport owing to the mesoporous structure.

6. Summary and perspective

This paper summarizes the recent progress and achievements in the soft-templating synthesis of mesoporous materials. First, we described the basic synthetic approaches, such as hard and soft templating methods, for fabricating mesoporous materials, as well as their (dis)advantages. Second, we discussed various compositions of mesoporous materials prepared by using the soft-templating method. Through the design of controllable synthesis conditions, such as self-assembly of SDAs and precursors, types of SDAs or precursors, and post-treatment, the soft-templating method has achieved tremendous progress in various applications with a wide range of mesoporous structures. Third, we summarized the various architectures of

mesoporous materials synthesized by new soft-templating methods. Finally, we discussed the recent progress of mesoporous materials for energy storage systems such as batteries and supercapacitors.

Despite notable achievements in soft-templating synthetic approaches, certain challenges and opportunities remain as follows. (i) In the synthesis of mesoporous materials, especially metal oxides and nitrides, the conversion from mesostructured composites to mesoporous materials relies on high-temperature thermal treatment, which restrict their direct integration on plastic substrates for flexible electrode applications. Therefore, innovative synthetic approaches capable of template removal while inducing the hydrolysis and condensation reactions of inorganic materials at low temperatures are highly required. (ii) Although great advances have been achieved in the synthesis of mesoporous materials with hierarchical structures, precise tailoring of the macrostructures of most hierarchical structures remains difficult. For example, hierarchical macro/mesoporous materials can be obtained using an SD of a polymer blend, but the resultant synthesized macroporous shape is not diverse and unpredictable. To expand the functionality of mesoporous materials, it is necessary to realize various macrostructures (complex architecture, sheets, spheres, and janus) by precisely controlling the formation of mesopores and macrostructure during self-assembly. (iii) For electrode applications for ESSs, mesoporous materials should have specific structures for satisfying high mass loading and effective loading of active materials in mesoporous materials. To achieve high mass loading on a current collector, spherical mesoporous particles with uniform size should be realized. In addition, for efficient interaction between the active materials and the electrolyte, active materials such as high-capacity active materials, alkali metals and sulfur, should be uniformly loaded into the conductive and physically/chemically stable mesopores without the restriction of electrolyte penetration. Therefore, efforts for the precisely controlled structures would attract great attention for high performance ESSs. In this regard, soft-templating methods have been effectively applied in various research fields because of the diversity of methods and structures.

Author contribution

K.-W. Kim designed and wrote the draft of the manuscript. B. Park and J. Kim helped to design the manuscript and to arrange figures and references. J. K. Kim and C. J. supervised and wrote the manuscript.

Conflicts of interest

There are no conflicts to declare.

Acknowledgements

This work was supported by the National Creative Research Initiative Program supported by the National Research Foundation of Korea (NRF) (grant no. 2022R1A3A3002149) funded by the Korean Government. This work was supported by the Korea Institute of Energy Technology Evaluation and Planning (KETEP) grant funded by the Korea Government (MOTIE) (20228510070100, development of long-life sodium ion batteries using a low-cost Prussian blue analogue).

References

1 C. Li, Q. Li, Y. V. Kaneti, D. Hou, Y. Yamauchi and Y. Mai, *Chem. Soc. Rev.*, 2020, **49**, 4681–4736.
2 E. Lim, C. Jo and J. Lee, *Nanoscale*, 2016, **8**, 7827–7833.
3 Y. Deng, J. Wei, Z. Sun and D. Zhao, *Chem. Soc. Rev.*, 2013, **42**, 4054–4070.
4 T. Kim, W. Song, D.-Y. Son, L. K. Ono and Y. Qi, *J. Mater. Chem. A*, 2019, **7**, 2942–2964.
5 M. R. Benzigar, S. N. Talapaneni, S. Joseph, K. Ramadass, G. Singh, J. Scaranto, U. Ravon, K. Al-Bahily and A. Vinu, *Chem. Soc. Rev.*, 2018, **47**, 2680–2721.
6 M. Peer, M. Lusardi and K. F. Jensen, *Chem. Mater.*, 2017, **29**, 1496–1506.
7 S. Yin, T. Tian, K. S. Wienhold, C. L. Weindl, R. Guo, M. Schwartzkopf, S. V. Roth and P. Müller-Buschbaum, *Adv. Mater. Interfaces*, 2020, **7**, 2001002.
8 K. Liang, W. Wang, Y. Yu, L. Liu, H. Lv, Y. Zhang and A. Chen, *New J. Chem.*, 2019, **43**, 2776–2782.
9 J. Cherusseri and K. K. Kar, *J. Mater. Chem. A*, 2016, **4**, 9910–9922.
10 N. K and C. S. Rout, *J. Mater. Chem. A*, 2021, **9**, 8248–8278.
11 J. Balach, J. Linnemann, T. Jaumann and L. Giebeler, *J. Mater. Chem. A*, 2018, **6**, 23127–23168.
12 H. Ao, Y. Zhao, J. Zhou, W. Cai, X. Zhang, Y. Zhu and Y. Qian, *J. Mater. Chem. A*, 2019, **7**, 18708–18734.
13 K.-W. Kim, T. Y. Yun, S.-H. You, X. Tang, J. Lee, Y. Seo, Y.-T. Kim, S. H. Kim, H. C. Moon and J. K. Kim, *NPG Asia Mater.*, 2020, **12**, 84.
14 L. Peng, Z. Fang, J. Li, L. Wang, A. M. Bruck, Y. Zhu, Y. Zhang, K. J. Takeuchi, A. C. Marschilok, E. A. Stach, E. S. Takeuchi and G. Yu, *ACS Nano*, 2018, **12**, 820–828.
15 J. Jiang, Y. Li, J. Liu, X. Huang, C. Yuan and X. W. Lou, *Adv. Mater.*, 2012, **24**, 5166–5180.
16 Y. Zou, X. Zhou, J. Ma, X. Yang and Y. Deng, *Chem. Soc. Rev.*, 2020, **49**, 1173–1208.
17 B. K. Wheatle, J. R. Hampton, G. G. Rodríguez-Calero, J. G. Werner, Y. Gu, U. Wiesner and H. D. Abruña, *J. Electroanal. Chem.*, 2020, **871**, 114284.
18 Q. Lu and Y. Zhou, *J. Power Sources*, 2011, **196**, 4088–4094.
19 M. R. Lukatskaya, S. Kota, Z. Lin, M.-Q. Zhao, N. Shpigel, M. D. Levi, J. Halim, P.-L. Taberna, M. W. Barsoum, P. Simon and Y. Gogotsi, *Nat. Energy*, 2017, **2**, 17105.
20 G. Feng, S. Li, V. Presser and P. T. Cummings, *J. Phys. Chem. Lett.*, 2013, **4**, 3367–3376.
21 Y. Wang, Y. Song and Y. Xia, *Chem. Soc. Rev.*, 2016, **45**, 5925–5950.
22 R. Ma, Z. Chen, D. Zhao, X. Zhang, J. Zhuo, Y. Yin, X. Wang, G. Yang and F. Yi, *J. Mater. Chem. A*, 2021, **9**, 11501–11529.
23 R. Wang, X. Yan, J. Lang, Z. Zheng and P. Zhang, *J. Mater. Chem. A*, 2014, **2**, 12724–12732.

24 M. Zhang, H. Mei, P. Chang and L. Cheng, *J. Mater. Chem. A*, 2020, **8**, 10670–10694.
25 Y. Yang, W. Wang, G. Meng and J. Zhang, *J. Mater. Chem. A*, 2022, **10**, 14137–14170.
26 Z. Zhou, T. Liu, A. U. Khan and G. Liu, *Sci. Adv.*, 2019, **5**, eaau6852.
27 Z. Li, K. Guo and X. Chen, *RSC Adv.*, 2017, **7**, 30521–30532.
28 K. Yan, L.-B. Kong, Y.-H. Dai, M. Shi, K.-W. Shen, B. Hu, Y.-C. Luo and L. Kang, *J. Mater. Chem. A*, 2015, **3**, 22781–22793.
29 Y. Liu, Z. Wang, W. Teng, H. Zhu, J. Wang, A. A. Elzatahry, D. Al-Dahyan, W. Li, Y. Deng and D. Zhao, *J. Mater. Chem. A*, 2018, **6**, 3162–3170.
30 C. Liang, Z. Li and S. Dai, *Angew. Chem., Int. Ed.*, 2008, **47**, 3696–3717.
31 J. Fan, X. Ran, Y. Ren, C. Wang, J. Yang, W. Teng, L. Zou, Y. Sun, B. Lu, Y. Deng and D. Zhao, *Langmuir*, 2016, **32**, 9922–9929.
32 H. Xiong, T. Gao, K. Li, Y. Liu, Y. Ma, J. Liu, Z.-A. Qiao, S. Song and S. Dai, *Adv. Sci.*, 2019, **6**, 1801543.
33 K. W. Tan, B. Jung, J. G. Werner, E. R. Rhoades, M. O. Thompson and U. Wiesner, *Science*, 2015, **349**, 54–58.
34 V. Velez, G. Ramos-Sánchez, B. Lopez, L. Lartundo-Rojas, I. González and L. Sierra, *Carbon*, 2019, **147**, 214–226.
35 Z. Su, C. Yang, C. Xu, H. Wu, Z. Zhang, T. Liu, C. Zhang, Q. Yang, B. Li and F. Kang, *J. Mater. Chem. A*, 2013, **1**, 12432–12440.
36 A. Singh and V. Kalra, *J. Mater. Chem. A*, 2019, **7**, 11613–11650.
37 E. Ramasamy, C. Jo, A. Anthonysamy, I. Jeong, J. K. Kim and J. Lee, *Chem. Mater.*, 2012, **24**, 1575–1582.
38 E. Ramasamy, J. Chun and J. Lee, *Carbon*, 2010, **48**, 4563–4565.
39 H. Qutaish, S. Tanaka, Y. V. Kaneti, J. Lin, Y. Bando, A. A. Alshehri, S.-I. Yusa, Y. Yamauchi, M. S. A. Hossain and J. Kim, *Microporous Mesoporous Mater.*, 2018, **271**, 16–22.
40 C. Jo, Y. Park, J. Jeong, K. T. Lee and J. Lee, *ACS Appl. Mater. Interfaces*, 2015, **7**, 11748–11754.
41 S. Shubhashish, A. S. Amin, Y. Dang, S. J. Karasik, H. S. Khanna and S. L. Suib, *ACS Appl. Nano Mater.*, 2022, **5**, 7078–7091.
42 E. Kamali-Heidari and A. Kamyabi-Gol, *Phys. Rev. B Condens. Matter*, 2019, **570**, 176–181.
43 A. S. Nugraha, V. Malgras, J. Kim, J. Bo, C. Li, M. Iqbal, Y. Yamauchi and T. Asahi, *Small Methods*, 2018, **2**, 1800283.
44 T. Soboleva, X. Zhao, K. Malek, Z. Xie, T. Navessin and S. Holdcroft, *ACS Appl. Mater. Interfaces*, 2010, **2**, 375–384.
45 Y. Wang, Y. Zhu, S. Chen and W. Li, *Energy Fuels*, 2014, **28**, 945–955.
46 Y. Gogotsi, A. Nikitin, H. Ye, W. Zhou, J. E. Fischer, B. Yi, H. C. Foley and M. W. Barsoum, *Nat. Mater.*, 2003, **2**, 591–594.
47 T. Kotaka, Y. Tabuchi and P. P. Mukherjee, *J. Power Sources*, 2015, **280**, 231–239.
48 V. Malgras, J. Tang, J. Wang, J. Kim, N. L. Torad, S. Dutta, K. Ariga, M. S. A. Hossain, Y. Yamauchi and K. C. W. Wu, *J. Nanosci. Nanotechnol.*, 2019, **19**, 3673–3685.
49 X. Ren, H. Li, J. Chen, L. Wei, A. Modak, H. Yang and Q. Yang, *Carbon*, 2017, **114**, 473–481.
50 L. Wu, Y. Li, Z. Fu and B.-L. Su, *Natl. Sci. Rev.*, 2020, **7**, 1667–1701.
51 K. J. De France, F. Xu and T. Hoare, *Adv. Healthc. Mater.*, 2018, **7**, 1700927.
52 Y. Ding, C. Wang, R. Zheng, S. Maitra, G. Zhang, T. Barakat, S. Roy, B.-L. Su and L.-H. Chen, *J. Energy Chem.*, 2022, **4**, 100081.
53 S. Lee, M. Choun, Y. Ye, J. Lee, Y. Mun, E. Kang, J. Hwang, Y.-H. Lee, C.-H. Shin, S.-H. Moon, S.-K. Kim, E. Lee and J. Lee, *Angew. Chem., Int. Ed.*, 2015, **54**, 9230–9234.
54 Y. Mun, M. J. Kim, S.-A. Park, E. Lee, Y. Ye, S. Lee, Y.-T. Kim, S. Kim, O.-H. Kim, Y.-H. Cho, Y.-E. Sung and J. Lee, *Appl. Catal., B*, 2018, **222**, 191–199.
55 M. G. Fischer, X. Hua, B. D. Wilts, I. Gunkel, T. M. Bennett and U. Steiner, *ACS Appl. Mater. Interfaces*, 2017, **9**, 22388–22397.
56 J. Hwang, C. Jo, M. G. Kim, J. Chun, E. Lim, S. Kim, S. Jeong, Y. Kim and J. Lee, *ACS Nano*, 2015, **9**, 5299–5309.
57 C. Xu, D. Niu, N. Zheng, H. Yu, J. He and Y. Li, *ACS Sustain. Chem. Eng.*, 2018, **6**, 5999–6007.
58 G. Lee, C. Lee, C.-M. Yoon, M. Kim and J. Jang, *ACS Appl. Mater. Interfaces*, 2017, **9**, 5222–5230.
59 Y. Qiu, M. Hou, J. Gao, H. Zhai, H. Liu, M. Jin, X. Liu and L. Lai, *Small*, 2019, **15**, 1903836.
60 T. Wagner, S. Haffer, C. Weinberger, D. Klaus and M. Tiemann, *Chem. Soc. Rev.*, 2013, **42**, 4036–4053.
61 Y. Shimizu, A. Jono, T. Hyodo and M. Egashira, *Sens. Actuators, B*, 2005, **108**, 56–61.
62 S. Zeng, S. Liu, Y. Qi, L. Cui, Q. Dai and C. Bai, *RSC Adv.*, 2018, **8**, 11462–11468.
63 W. Zhang, R.-r. Cheng, H.-h. Bi, Y.-h. Lu, L.-b. Ma and X.-j. He, *New Carbon Mater.*, 2021, **36**, 69–81.
64 T. Ghoshal, A. Thorat, N. Prochukhan and M. A. Morris, *Nanomaterials*, 2022, **12**, 2223.
65 J. Lee, R. Nankya, A. Kim and H. Jung, *Electrochim. Acta*, 2018, **290**, 496–505.
66 J. Lee, M. Kang, I.-K. Shim, D. H. Lee, A. Kim and H. Jung, *J. Nanosci. Nanotechnol.*, 2018, **18**, 6995–7003.
67 J. Wei, D. Zhou, Z. Sun, Y. Deng, Y. Xia and D. Zhao, *Adv. Funct. Mater.*, 2013, **23**, 2322–2328.
68 J. Zhang, Y. Deng, D. Gu, S. Wang, L. She, R. Che, Z.-S. Wang, B. Tu, S. Xie and D. Zhao, *Adv. Energy Mater.*, 2011, **1**, 241–248.
69 T. Matsuno, Y. Kuroda, M. Kitahara, A. Shimojima, H. Wada and K. Kuroda, *Angew. Chem., Int. Ed.*, 2016, **55**, 6008–6012.
70 Q. Wu, C. Liu, J. Peng and F. Liu, *RSC Adv.*, 2017, **7**, 19557–19564.
71 Z. Wu, Q. Li, D. Feng, P. A. Webley and D. Zhao, *J. Am. Chem. Soc.*, 2010, **132**, 12042–12050.

72 P. Strubel, S. Thieme, T. Biemelt, A. Helmer, M. Oschatz, J. Brückner, H. Althues and S. Kaskel, *Adv. Funct. Mater.*, 2015, **25**, 287–297.
73 M. R. J. Scherer, L. Li, P. M. S. Cunha, O. A. Scherman and U. Steiner, *Adv. Mater.*, 2012, **24**, 1217–1221.
74 L. Xiang, S. Yuan, F. Wang, Z. Xu, X. Li, F. Tian, L. Wu, W. Yu and Y. Mai, *J. Am. Chem. Soc.*, 2022, **144**, 15497–15508.
75 Y. La, J. Song, M. G. Jeong, A. Cho, S.-M. Jin, E. Lee and K. T. Kim, *Nat. Commun.*, 2018, **9**, 5327.
76 S. Tanaka, N. Nishiyama, Y. Egashira and K. Ueyama, *Chem. Commun.*, 2005, **16**, 2125–2127.
77 M. Trivedi, F. Peng, X. Xia, P. I. Sepulveda-Medina and B. D. Vogt, *Langmuir*, 2019, **35**, 14049–14059.
78 H.-F. Fei, Y. Long, H.-J. Yu, B. M. Yavitt, W. Fan, A. Ribbe and J. J. Watkins, *ACS Appl. Mater. Interfaces*, 2020, **12**, 57322–57329.
79 J. Choma, J. Jagiello and M. Jaroniec, *Carbon*, 2021, **183**, 150–157.
80 D. Fattakhova-Rohlfing, M. Wark, T. Brezesinski, B. M. Smarsly and J. Rathouský, *Adv. Funct. Mater.*, 2007, **17**, 123–132.
81 T. Lunkenbein, M. Kamperman, M. Schieder, S. With, Z. Li, H. Sai, S. Förster, U. Wiesner and J. Breu, *J. Mater. Chem. A*, 2013, **1**, 6238–6248.
82 T. M. Bennett, G. He, R. R. Larder, M. G. Fischer, G. A. Rance, M. W. Fay, A. K. Pearce, C. D. J. Parmenter, U. Steiner and S. M. Howdle, *Nano Lett.*, 2018, **18**, 7560–7569.
83 F. Meng, Z. Fang, Z. Li, W. Xu, M. Wang, Y. Liu, J. Zhang, W. Wang, D. Zhao and X. Guo, *J. Mater. Chem. A*, 2013, **1**, 7235–7241.
84 W.-C. Chu, B. P. Bastakoti, Y. V. Kaneti, J.-G. Li, H. R. Alamri, Z. A. Alothman, Y. Yamauchi and S.-W. Kuo, *Eur. J. Chem.*, 2017, **23**, 13734–13741.
85 Y. Oka, Y. Kuroda, T. Matsuno, K. Kamata, H. Wada, A. Shimojima and K. Kuroda, *Eur. J. Chem.*, 2017, **23**, 9362–9368.
86 J. Wei, Z. Sun, W. Luo, Y. Li, A. A. Elzatahry, A. M. Al-Enizi, Y. Deng and D. Zhao, *J. Am. Chem. Soc.*, 2017, **139**, 1706–1713.
87 Y. Zou, X. Zhou, Y. Zhu, X. Cheng, D. Zhao and Y. Deng, *Acc. Chem. Res.*, 2019, **52**, 714–725.
88 T. Nagaura, H.-P. Phan, V. Malgras, T.-A. Pham, H. Lim, A. Ashok, J. Kim, J. You, N.-T. Nguyen, J. Na and Y. Yamauchi, *Angew. Chem., Int. Ed.*, 2021, **60**, 9660–9665.
89 O. Olatidoye, D. Thomas and B. P. Bastakoti, *New J. Chem.*, 2021, **45**, 15761–15766.
90 P. Li, Y. Feng, D. Cheng and J. Wei, *J. Colloid Interface Sci.*, 2022, **625**, 435–445.
91 B. P. Bastakoti, S. Ishihara, S.-Y. Leo, K. Ariga, K. C. W. Wu and Y. Yamauchi, *Langmuir*, 2014, **30**, 651–659.
92 Y. Li, W. Luo, N. Qin, J. Dong, J. Wei, W. Li, S. Feng, J. Chen, J. Xu, A. A. Elzatahry, M. H. Es-Saheb, Y. Deng and D. Zhao, *Angew. Chem., Int. Ed.*, 2014, **53**, 9035–9040.
93 W. S. Chi, C. S. Lee, H. Long, M. H. Oh, A. Zettl, C. Carraro, J. H. Kim and R. Maboudian, *ACS Appl. Mater. Interfaces*, 2017, **9**, 37246–37253.
94 S. Tanaka, B. P. Bastakoti, Y. L. S.-i. Yusa, D. Ishii, K. Kani, A. Fatehmulla, W. A. Farooq, M. J. A. Shiddiky, Y. Bando, Y. V. Kaneti, Y. Yamauchi and M. S. A. Hossain, *Eur. J. Inorg. Chem.*, 2017, **2017**, 1328–1332.
95 X. Xiao, L. Liu, J. Ma, Y. Ren, X. Cheng, Y. Zhu, D. Zhao, A. A. Elzatahry, A. Alghamdi and Y. Deng, *ACS Appl. Mater. Interfaces*, 2018, **10**, 1871–1880.
96 V. Malgras, Y. Shirai, T. Takei and Y. Yamauchi, *J. Am. Chem. Soc.*, 2020, **142**, 15815–15822.
97 A. Balint, M. Papendick, M. Clauss, C. Müller, F. Giesselmann and S. Naumann, *Chem. Commun.*, 2018, **54**, 2220–2223.
98 F. Markus, J. R. Bruckner and S. Naumann, *Macromol. Chem. Phys.*, 2020, **221**, 1900437.
99 J. Shim, J. Lee, Y. Ye, J. Hwang, S.-K. Kim, T.-H. Lim, U. Wiesner and J. Lee, *ACS Nano*, 2012, **6**, 6870–6881.
100 T. Liu, J. Serrano, J. Elliott, X. Yang, W. Cathcart, Z. Wang, Z. He and G. Liu, *Sci. Adv.*, 2020, **6**, eaaz0906.
101 A. A. S. Gonçalves and M. Jaroniec, *J. Colloid Interface Sci.*, 2019, **537**, 725–735.
102 Y. Ren, X. Yang, X. Zhou, W. Luo, Y. Zhang, X. Cheng and Y. Deng, *Chin. Chem. Lett.*, 2019, **30**, 2003–2008.
103 J. Hwang, S. Kim, U. Wiesner and J. Lee, *Adv. Mater.*, 2018, **30**, 1801127.
104 A. Fischer, M. Antonietti and A. Thomas, *Adv. Mater.*, 2007, **19**, 264–267.
105 W.-G. Lim, C. Jo, A. Cho, J. Hwang, S. Kim, J. W. Han and J. Lee, *Adv. Mater.*, 2019, **31**, 1806547.
106 J. Shi, H. Cui, J. Xu, N. Yan and Y. Liu, *Chem. Eng. J.*, 2020, **389**, 124459.
107 Y. Mun, J. Shim, K. Kim, J. W. Han, S.-K. Kim, Y. Ye, J. Hwang, S. Lee, J. Jang, Y.-T. Kim and J. Lee, *RSC Adv.*, 2016, **6**, 88255–88264.
108 H.-S. Hsueh, C.-T. Yang, J. I. Zink and M. H. Huang, *J. Phys. Chem. B*, 2005, **109**, 4404–4409.
109 K. Brezesinski, J. Haetge, J. Wang, S. Mascotto, C. Reitz, A. Rein, S. H. Tolbert, J. Perlich, B. Dunn and T. Brezesinski, *Small*, 2011, **7**, 407–414.
110 F. Yu, R. P. Thedford, K. R. Hedderick, G. Freychet, M. Zhernenkov, L. A. Estroff, K. C. Nowack, S. M. Gruner and U. B. Wiesner, *ACS Appl. Mater. Interfaces*, 2021, **13**, 34732–34741.
111 B. T. Sone, S. S. Nkosi, M. M. Nkosi, E. Coetsee-Hugo, H. C. Swart and M. Maaza, *AIP Conf. Proc.*, 2018, **1962**, 040003.
112 T. W. Hansen, A. T. DeLaRiva, S. R. Challa and A. K. Datye, *Acc. Chem. Res.*, 2013, **46**, 1720–1730.
113 M. S. Song, S. Nahm, W. I. Cho and C. Lee, *Phys. Chem. Chem. Phys.*, 2015, **17**, 23496–23502.
114 L. Almar, T. Andreu, A. Morata, M. Torrell, L. Yedra, S. Estradé, F. Peiró and A. Tarancón, *J. Mater. Chem. A*, 2014, **2**, 3134–3141.

115 Y. Ito, Y. Tanabe, H. J. Qiu, K. Sugawara, S. Heguri, N. H. Tu, K. K. Huynh, T. Fujita, T. Takahashi, K. Tanigaki and M. Chen, *Angew. Chem.*, 2014, **126**, 4922–4926.
116 F. Markus, C. Vogler, J. R. Bruckner and S. Naumann, *ACS Appl. Nano Mater.*, 2021, **4**, 3486–3492.
117 Y. Deng, T. Yu, Y. Wan, Y. Shi, Y. Meng, D. Gu, L. Zhang, Y. Huang, C. Liu, X. Wu and D. Zhao, *J. Am. Chem. Soc.*, 2007, **129**, 1690–1697.
118 W. Zhong, T. Jiang, T. Jafari, A. S. Poyraz, W. Wu, D. A. Kriz, S. Du, S. Biswas, M. Thompson Pettes and S. L. Suib, *Microporous Mesoporous Mater.*, 2017, **239**, 328–335.
119 S.-z. Niu, S.-d. Wu, W. Lu, Q.-h. Yang and F.-y. Kang, *New Carbon Mater.*, 2017, **32**, 289–296.
120 X. Deng, K. Chen and H. Tüysüz, *Chem. Mater.*, 2017, **29**, 40–52.
121 W. Luc and F. Jiao, *Acc. Chem. Res.*, 2016, **49**, 1351–1358.
122 Z. Liu, C. Li, M. Kuang, B. Liu and B. Yang, *Environ. Sci. Pollut. Res.*, 2021, **28**, 31630–31639.
123 Z. Zhang, Y. Zhu, H. Asakura, B. Zhang, J. Zhang, M. Zhou, Y. Han, T. Tanaka, A. Wang, T. Zhang and N. Yan, *Nat. Commun.*, 2017, **8**, 16100.
124 C. Wang, Y. Zhao, L. Zhou, Y. Liu, W. Zhang, Z. Zhao, W. N. Hozzein, H. M. S. Alharbi, W. Li and D. Zhao, *J. Mater. Chem. A*, 2018, **6**, 21550–21557.
125 Y. Dong, X. Zhan, X. Niu, J. Li, F. Yuan, Y. Zhu and H. Fu, *Microporous Mesoporous Mater.*, 2014, **185**, 97–106.
126 B. E. Wilson, S. G. Rudisill and A. Stein, *Microporous Mesoporous Mater.*, 2014, **197**, 174–179.
127 K. Nanaji, A. Jyothirmayi, U. Varadaraju, T. N. Rao and S. Anandan, *J. Alloys Compd.*, 2017, **723**, 488–497.
128 J. H. Pan, X. S. Zhao and W. I. Lee, *Chem. Eng. J.*, 2011, **170**, 363–380.
129 C. T. Kresge, M. E. Leonowicz, W. J. Roth, J. C. Vartuli and J. S. Beck, *Nature*, 1992, **359**, 710–712.
130 J. S. Beck, J. C. Vartuli, W. J. Roth, M. E. Leonowicz, C. T. Kresge, K. D. Schmitt, C. T. W. Chu, D. H. Olson, E. W. Sheppard, S. B. McCullen, J. B. Higgins and J. L. Schlenker, *J. Am. Chem. Soc.*, 1992, **114**, 10834–10843.
131 Y. Wan, Y. Shi and D. Zhao, *Chem. Commun.*, 2007, **9**, 897–926.
132 Y. Wan and D. Zhao, *Chem. Rev.*, 2007, **107**, 2821–2860.
133 D. Zhao, J. Feng, Q. Huo, N. Melosh, G. H. Fredrickson, B. F. Chmelka and G. D. Stucky, *Science*, 1998, **279**, 548–552.
134 J. Shi, N. Lin, H.-b. Lin, J. Yang and W.-l. Zhang, *New Carbon Mater.*, 2020, **35**, 401–409.
135 S. Zhu, H. Tian, N. Wang, B. Chen, Y. Mai and X. Feng, *Small*, 2018, **14**, 1702755.
136 D. Hou, J. Zhang, H. Tian, Q. Li, C. Li and Y. Mai, *Adv. Mater. Interfaces*, 2019, **6**, 1901476.
137 J. Lee, M. Christopher Orilall, S. C. Warren, M. Kamperman, F. J. DiSalvo and U. Wiesner, *Nat. Mater.*, 2008, **7**, 222–228.
138 H. Wakayama, H. Yonekura and Y. Kawai, *Int. J. Nanotechnol.*, 2018, **15**, 798–803.
139 C. Jo, W.-G. Lim, A. H. Dao, S. Kim, S. Kim, S. Yoon and J. Lee, *J. Mater. Chem. A*, 2017, **5**, 24782–24789.
140 S. Choudhury, M. Agrawal, P. Formanek, D. Jehnichen, D. Fischer, B. Krause, V. Albrecht, M. Stamm and L. Ionov, *ACS Nano*, 2015, **9**, 6147–6157.
141 B. Xu, F. Wu, D. Mu, L. Dai, G. Cao, H. Zhang, S. Chen and Y. Yang, *Int. J. Hydrogen Energy*, 2010, **35**, 632–637.
142 J. G. Werner, G. G. Rodríguez-Calero, H. D. Abruña and U. Wiesner, *Energy Environ. Sci.*, 2018, **11**, 1261–1270.
143 Y. Korenblit, M. Rose, E. Kockrick, L. Borchardt, A. Kvit, S. Kaskel and G. Yushin, *ACS Nano*, 2010, **4**, 1337–1344.
144 T. N. Phan, M. K. Gong, R. Thangavel, Y. S. Lee and C. H. Ko, *J. Alloys Compd.*, 2019, **780**, 90–97.
145 S. Kim, M. Ju, J. Lee, J. Hwang and J. Lee, *J. Am. Chem. Soc.*, 2020, **142**, 9250–9257.
146 Y. Meng, D. Gu, F. Zhang, Y. Shi, H. Yang, Z. Li, C. Yu, B. Tu and D. Zhao, *Angew. Chem., Int. Ed.*, 2005, **44**, 7053–7059.
147 R. Liu, Y. Shi, Y. Wan, Y. Meng, F. Zhang, D. Gu, Z. Chen, B. Tu and D. Zhao, *J. Am. Chem. Soc.*, 2006, **128**, 11652–11662.
148 A. Zhang, A. Li, Y. Wang, M. Liu, H. Ma, Z. Song and J. Liu, *RSC Adv.*, 2016, **6**, 103843–103850.
149 J. M. Serrano, T. Liu, A. U. Khan, B. Botset, B. J. Stovall, Z. Xu, D. Guo, K. Cao, X. Hao, S. Cheng and G. Liu, *Chem. Mater.*, 2019, **31**, 8898–8907.
150 T. Liu, Z. Zhou, Y. Guo, D. Guo and G. Liu, *Nat. Commun.*, 2019, **10**, 675.
151 Z. Zhou, T. Liu, A. U. Khan and G. Liu, *Mol. Syst. Des. Eng.*, 2020, **5**, 153–165.
152 A. F. M. El-Mahdy, T.-E. Liu and S.-W. Kuo, *J. Hazard. Mater.*, 2020, **391**, 122163.
153 X. Yang, H. Ma and G. Zhang, *Langmuir*, 2017, **33**, 3975–3981.
154 E. Kang, Y. S. Jung, G.-H. Kim, J. Chun, U. Wiesner, A. C. Dillon, J. K. Kim and J. Lee, *Adv. Funct. Mater.*, 2011, **21**, 4349–4357.
155 C. Jo, Y. Kim, J. Hwang, J. Shim, J. Chun and J. Lee, *Chem. Mater.*, 2014, **26**, 3508–3514.
156 X. Yang, X. Cheng, J. Ma, Y. Zou, W. Luo and Y. Deng, *Small*, 2019, **15**, 1903058.
157 K. Yu, A. J. Hurd, A. Eisenberg and C. J. Brinker, *Langmuir*, 2001, **17**, 7961–7965.
158 K. Yu, B. Smarsly and C. J. Brinker, *Adv. Funct. Mater.*, 2003, **13**, 47–52.
159 P. Yang, D. Zhao, D. I. Margolese, B. F. Chmelka and G. D. Stucky, *Nature*, 1998, **396**, 152–155.
160 P. Yang, D. Zhao, D. I. Margolese, B. F. Chmelka and G. D. Stucky, *Chem. Mater.*, 1999, **11**, 2813–2826.
161 H. Xiong, H. Zhou, C. Qi, Z. Liu, L. Zhang, L. Zhang and Z.-A. Qiao, *Chem. Eng. J.*, 2020, **398**, 125527.
162 J. Hwang, J. Kim, E. Ramasamy, W. Choi and J. Lee, *Microporous Mesoporous Mater.*, 2011, **143**, 149–156.
163 D. Xu, K. Ge, S. Qi, Y. Chen, J. Qiu, S. Wang, Y. Tian, S. Fang, C. Liu and Q. Liu, *J. Mater. Sci.*, 2020, **55**, 7645–7651.
164 J. Lee, J. Kim and T. Hyeon, *Adv. Mater.*, 2006, **18**, 2073–2094.
165 Z. Wang, Y. Zhu, W. Luo, Y. Ren, X. Cheng, P. Xu, X. Li, Y. Deng and D. Zhao, *Chem. Mater.*, 2016, **28**, 7773–7780.

166 Y. Zhu, Y. Zhao, J. Ma, X. Cheng, J. Xie, P. Xu, H. Liu, H. Liu, H. Zhang, M. Wu, A. A. Elzatahry, A. Alghamdi, Y. Deng and D. Zhao, *J. Am. Chem. Soc.*, 2017, **139**, 10365–10373.
167 D. Feng, T.-N. Gao, M. Fan, A. Li, K. Li, T. Wang, Q. Huo and Z.-A. Qiao, *NPG Asia Mater.*, 2018, **10**, 800–809.
168 B. Eckhardt, E. Ortel, D. Bernsmeier, J. Polte, P. Strasser, U. Vainio, F. Emmerling and R. Kraehnert, *Chem. Mater.*, 2013, **25**, 2749–2758.
169 W. Luo, Y. Li, J. Dong, J. Wei, J. Xu, Y. Deng and D. Zhao, *Angew. Chem., Int. Ed.*, 2013, **52**, 10505–10510.
170 S. Kim, C. Choi, J. Hwang, J. Park, J. Jeong, H. Jun, S. Lee, S.-K. Kim, J. H. Jang, Y. Jung and J. Lee, *ACS Nano*, 2020, **14**, 4988–4999.
171 B. L. Cushing, V. L. Kolesnichenko and C. J. O'Connor, *Chem. Rev.*, 2004, **104**, 3893–3946.
172 A. E. Danks, S. R. Hall and Z. Schnepp, *Mater. Horiz.*, 2016, **3**, 91–112.
173 G. J. d. A. A. Soler-Illia, C. Sanchez, B. Lebeau and J. Patarin, *Chem. Rev.*, 2002, **102**, 4093–4138.
174 X. Zhang, M. Wang, G. Zhu, D. Li, D. Yan, T. Lu and L. Pan, *Ceram. Int.*, 2017, **43**, 2398–2402.
175 J. N. Kondo, Y. Hiyoshi, R. Osuga, A. Ishikawa, Y.-H. Wang and T. Yokoi, *Microporous Mesoporous Mater.*, 2018, **262**, 191–198.
176 U. Mgwetyana, M. Elizabeth Makhatha, M. Mamo and P. Ndungu, *Mater. Today: Proc.*, 2018, **5**, 10585–10591.
177 S. Tanaka, Y. V. Kaneti, R. Bhattacharjee, M. N. Islam, R. Nakahata, N. Abdullah, S.-i. Yusa, N.-T. Nguyen, M. J. A. Shiddiky, Y. Yamauchi and M. S. A. Hossain, *ACS Appl. Mater. Interfaces*, 2018, **10**, 1039–1049.
178 R. Azoulay, N. Shomrat, I. Weisbord, G. Atiya and T. Segal-Peretz, *Small*, 2019, **15**, 1904657.
179 B. K. Barick, A. Simon, I. Weisbord, N. Shomrat and T. Segal-Peretz, *J. Colloid Interface Sci.*, 2019, **557**, 537–545.
180 D. H. Yi, C.-Y. Nam, G. Doerk, C. T. Black and R. B. Grubbs, *ACS Appl. Bio Mater.*, 2019, **1**, 672–683.
181 Y. Wang, N. Li, C. Hou, B. He, J. Li, F. Dang, J. Wang and Y. Fan, *Ceram. Int.*, 2020, **46**, 9119–9128.
182 G. He, P. Wang, K. Feng, H. Dong, H. Zhao, F. Sun, H. Yin, W. Li and G. Li, *Macromolecules*, 2021, **54**, 906–918.
183 L. Tang, B. Han, K. Persson, C. Friesen, T. He, K. Sieradzki and G. Ceder, *J. Am. Chem. Soc.*, 2010, **132**, 596–600.
184 L. Tang, X. Li, R. C. Cammarata, C. Friesen and K. Sieradzki, *J. Am. Chem. Soc.*, 2010, **132**, 11722–11726.
185 X. Zhang, N. Peng, T. Liu, R. Zheng, M. Xia, H. Yu, S. Chen, M. Shui and J. Shu, *Nano Energy*, 2019, **65**, 104049.
186 Y.-P. Zhu, T.-Z. Ren and Z.-Y. Yuan, *Catal. Sci. Technol.*, 2015, **5**, 4258–4279.
187 V. Malgras, H. Ataee-Esfahani, H. Wang, B. Jiang, C. Li, K. C. W. Wu, J. H. Kim and Y. Yamauchi, *Adv. Mater.*, 2016, **28**, 993–1010.
188 Y. Yamauchi, M. Komatsu, A. Takai, R. Sebata, M. Sawada, T. Momma, M. Fuziwara, T. Osaka and K. Kuroda, *Electrochim. Acta*, 2007, **53**, 604–609.
189 Y. Yamauchi and K. Kuroda, *Chem.–Asian J.*, 2008, **3**, 664–676.
190 L. Palanikumar, E. S. Choi, J. Y. Cheon, S. H. Joo and J.-H. Ryu, *Adv. Funct. Mater.*, 2015, **25**, 957–965.
191 E. N. Kusumawati and T. Sasaki, *Chem. Rec.*, 2019, **19**, 2058–2068.
192 S. C. Warren, L. C. Messina, L. S. Slaughter, M. Kamperman, Q. Zhou, S. M. Gruner, F. J. DiSalvo and U. Wiesner, *Science*, 2008, **320**, 1748–1752.
193 Z. Li, K. Hur, H. Sai, T. Higuchi, A. Takahara, H. Jinnai, S. M. Gruner and U. Wiesner, *Nat. Commun.*, 2014, **5**, 3247.
194 C. Li, Ö. Dag, T. D. Dao, T. Nagao, Y. Sakamoto, T. Kimura, O. Terasaki and Y. Yamauchi, *Nat. Commun.*, 2015, **6**, 6608.
195 B. Jiang, C. Li, Ö. Dag, H. Abe, T. Takei, T. Imai, M. S. A. Hossain, M. T. Islam, K. Wood, J. Henzie and Y. Yamauchi, *Nat. Commun.*, 2017, **8**, 15581.
196 J. Mondal, P. Borah, A. Modak, Y. Zhao and A. Bhaumik, *Org. Process Res. Dev.*, 2014, **18**, 257–265.
197 L. Wang, Y. Nemoto and Y. Yamauchi, *J. Am. Chem. Soc.*, 2011, **133**, 9674–9677.
198 P. Karthika, H. Ataee-Esfahani, Y.-H. Deng, K. C. W. Wu, N. Rajalakshmi, K. S. Dhathathreyan, D. Arivuoli, K. Ariga and Y. Yamauchi, *Chem. Lett.*, 2013, **42**, 447–449.
199 Y. Kuroda, Y. Yamauchi and K. Kuroda, *Chem. Commun.*, 2010, **46**, 1827–1829.
200 S. Guo, S. Dong and E. Wang, *ACS Nano*, 2010, **4**, 547–555.
201 Z. Zhang, Y. Yang, F. Nosheen, P. Wang, J. Zhang, J. Zhuang and X. Wang, *Small*, 2013, **9**, 3063–3069.
202 Y. Shi, Y. Wan, R. Zhang and D. Zhao, *Adv. Funct. Mater.*, 2008, **18**, 2436–2443.
203 S. W. Robbins, H. Sai, F. J. DiSalvo, S. M. Gruner and U. Wiesner, *ACS Nano*, 2014, **8**, 8217–8223.
204 P. A. Beaucage, E. M. Susca, S. M. Gruner and U. B. Wiesner, *Chem. Mater.*, 2017, **29**, 8973–8977.
205 B. G. Kim, C. Jo, J. Shin, Y. Mun, J. Lee and J. W. Choi, *ACS Nano*, 2017, **11**, 1736–1746.
206 K. E. Fritz, P. A. Beaucage, F. Matsuoka, U. Wiesner and J. Suntivich, *Chem. Commun.*, 2017, **53**, 7250–7253.
207 C. Jo, J. Hwang, W.-G. Lim, J. Lim, K. Hur and J. Lee, *Adv. Mater.*, 2018, **30**, 1703829.
208 J. Wang, J. Tang, B. Ding, V. Malgras, Z. Chang, X. Hao, Y. Wang, H. Dou, X. Zhang and Y. Yamauchi, *Nat. Commun.*, 2017, **8**, 15717.
209 S. A. Hesse, K. E. Fritz, P. A. Beaucage, R. P. Thedford, F. Yu, F. J. DiSalvo, J. Suntivich and U. Wiesner, *ACS Nano*, 2020, **14**, 16897–16906.
210 C. M. A. Parlett, M. A. Isaacs, S. K. Beaumont, L. M. Bingham, N. S. Hondow, K. Wilson and A. F. Lee, *Nat. Mater.*, 2016, **15**, 178–182.
211 Y. Li, X. Zhou, W. Luo, X. Cheng, Y. Zhu, A. M. El-Toni, A. Khan, Y. Deng and D. Zhao, *Adv. Mater. Interfaces*, 2019, **6**, 1801269.
212 N. D. Petkovich and A. Stein, *Chem. Soc. Rev.*, 2013, **42**, 3721–3739.
213 Y. Hu, X. Wang, M. Zhang, S. Wang, S. Li and G. Chen, *Nano Lett.*, 2021, **21**, 250–257.
214 D. Lee, J.-Y. Jung, M.-J. Jung and Y.-S. Lee, *Chem. Eng. J.*, 2015, **263**, 62–70.

215 H. Sai, K. W. Tan, K. Hur, E. Asenath-Smith, R. Hovden, Y. Jiang, M. Riccio, D. A. Muller, V. Elser, L. A. Estroff, S. M. Gruner and U. Wiesner, *Science*, 2013, **341**, 530–534.
216 J. Hwang, C. Jo, K. Hur, J. Lim, S. Kim and J. Lee, *J. Am. Chem. Soc.*, 2014, **136**, 16066–16072.
217 S. Kim, I. Jeong, J. Hwang, M. J. Ko and J. Lee, *Chem. Commun.*, 2017, **53**, 4100–4103.
218 W. Zhu, S. Tao, C.-a. Tao, W. Li, C. Lin, M. Li, Y. Wen and G. Li, *Langmuir*, 2011, **27**, 8451–8457.
219 F. Li, Z. Wang, N. S. Ergang, C. A. Fyfe and A. Stein, *Langmuir*, 2007, **23**, 3996–4004.
220 J. Du, X. Lai, N. Yang, J. Zhai, D. Kisailus, F. Su, D. Wang and L. Jiang, *ACS Nano*, 2011, **5**, 590–596.
221 H.-J. Liu, X.-M. Wang, W.-J. Cui, Y.-Q. Dou, D.-Y. Zhao and Y.-Y. Xia, *J. Mater. Chem.*, 2010, **20**, 4223–4230.
222 S. Kim, J. Hwang, J. Lee and J. Lee, *Sci. Adv.*, 2020, **6**, eabb3814.
223 S. Liu, P. Gordiichuk, Z.-S. Wu, Z. Liu, W. Wei, M. Wagner, N. Mohamed-Noriega, D. Wu, Y. Mai, A. Herrmann, K. Müllen and X. Feng, *Nat. Commun.*, 2015, **6**, 8817.
224 N. Devabharathi, S. K. Mondal and S. Dasgupta, *Nanoscale*, 2019, **11**, 13731–13740.
225 E. Shukrun Farrell, Y. Schilt, M. Y. Moshkovitz, Y. Levi-Kalisman, U. Raviv and S. Magdassi, *Nano Lett.*, 2020, **20**, 6598–6605.
226 C. Li, C. Jiang, Y. Deng, T. Li, N. Li, M. Peng and J. Wang, *Sci. Rep.*, 2017, **7**, 41331.
227 Z. Wang, Y. Wang, J. Yan, K. Zhang, F. Lin, L. Xiang, L. Deng, Z. Guan, W. Cui and H. Zhang, *Adv. Drug Deliv. Rev*, 2021, **174**, 504–534.
228 P. Pei, Z. Tian and Y. Zhu, *Microporous Mesoporous Mater.*, 2018, **272**, 24–30.
229 F. Putz, S. Scherer, M. Ober, R. Morak, O. Paris and N. Hüsing, *Adv. Mater. Technol.*, 2018, **3**, 1800060.
230 D.-S. Moon and J.-K. Lee, *Langmuir*, 2012, **28**, 12341–12347.
231 X. Zuo, Y. Xia, Q. Ji, X. Gao, S. Yin, M. Wang, X. Wang, B. Qiu, A. Wei, Z. Sun, Z. Liu, J. Zhu and Y.-J. Cheng, *ACS Nano*, 2017, **11**, 889–899.
232 Y. Yan, G. Chen, P. She, G. Zhong, W. Yan, B. Y. Guan and Y. Yamauchi, *Adv. Mater.*, 2020, **32**, 2004654.
233 K.-W. Kim, J. Kim, C. Choi, H. K. Yoon, M. C. Go, J. Lee, J. K. Kim, H. Seok, T. Kim, K. Wu, S. H. Kim, Y. M. Kim, J. H. Kwon and H. C. Moon, *ACS Appl. Mater. Interfaces*, 2022, **14**, 46994–47002.
234 J. Xu, Y. Dou, Z. Wei, J. Ma, Y. Deng, Y. Li, H. Liu and S. Dou, *Adv. Sci.*, 2017, **4**, 1700146.
235 G. He, B. Mandlmeier, J. Schuster, L. F. Nazar and T. Bein, *Chem. Mater.*, 2014, **26**, 3879–3886.
236 N. Nitta, F. Wu, J. T. Lee and G. Yushin, *Mater. Today*, 2015, **18**, 252–264.
237 L. Wang, Y. Lu, J. Liu, M. Xu, J. Cheng, D. Zhang and J. B. Goodenough, *Angew. Chem.*, 2013, **125**, 2018–2021.
238 T. Hosaka, K. Kubota, A. S. Hameed and S. Komaba, *Chem. Rev.*, 2020, **120**, 6358–6466.
239 S. Gheytani, Y. Liang, F. Wu, Y. Jing, H. Dong, K. K. Rao, X. Chi, F. Fang and Y. Yao, *Adv. Sci.*, 2017, **4**, 1700465.
240 J. Niu, Z. Zhang and D. Aurbach, *Adv. Energy Mater.*, 2020, **10**, 2000697.
241 M. Song, H. Tan, D. Chao and H. J. Fan, *Adv. Funct. Mater.*, 2018, **28**, 1802564.
242 G. A. Elia, K. V. Kravchyk, M. V. Kovalenko, J. Chacón, A. Holland and R. G. A. Wills, *J. Power Sources*, 2021, **481**, 228870.
243 S. Kim, W.-G. Lim, H. Im, M. Ban, J. W. Han, J. Lee, J. Hwang and J. Lee, *J. Am. Chem. Soc.*, 2021, **143**, 15644–15652.
244 Y. Li, C. Wu, Y. Bai, L. Liu, H. Wang, F. Wu, N. Zhang and Y. Zou, *ACS Appl. Mater. Interfaces*, 2016, **8**, 18832–18840.
245 C. Liu, Z. G. Neale and G. Cao, *Mater. Today*, 2016, **19**, 109–123.
246 G. Wang, H. Liu, J. Liu, S. Qiao, G. M. Lu, P. Munroe and H. Ahn, *Adv. Mater.*, 2010, **22**, 4944–4948.
247 F. Jiao, J. Bao, A. H. Hill and P. G. Bruce, *Angew. Chem., Int. Ed.*, 2008, **47**, 9711–9716.
248 C. Chen, H. Xu, B. Zhang, Q. Jiang, Y. Zhang, L. Li and Z. Lin, *Chem. Commun.*, 2020, **56**, 786–789.
249 H. Tian, H. Tian, S. Wang, S. Chen, F. Zhang, L. Song, H. Liu, J. Liu and G. Wang, *Nat. Commun.*, 2020, **11**, 5025.
250 K.-H. Kwak, H. J. Suh, A. Kim, S. Park, J. Song, S. Li, Y. Kim, G. Jeong, H. Kim and Y.-J. Kim, *Nano Energy*, 2019, **66**, 104138.
251 J. Zhang, X. Zhou, Y. Wang, J. Qian, F. Zhong, X. Feng, W. Chen, X. Ai, H. Yang and Y. Cao, *Small*, 2019, **15**, 1903723.
252 Y. Xu, Y. Zhu and C. Wang, *J. Mater. Chem. A*, 2014, **2**, 9751–9757.
253 J. Jeong, J. Chun, W.-G. Lim, W. B. Kim, C. Jo and J. Lee, *Nanoscale*, 2020, **12**, 11818–11824.
254 R. Mo, F. Li, X. Tan, P. Xu, R. Tao, G. Shen, X. Lu, F. Liu, L. Shen, B. Xu, Q. Xiao, X. Wang, C. Wang, J. Li, G. Wang and Y. Lu, *Nat. Commun.*, 2019, **10**, 1474.
255 K. Lan, Y. Liu, W. Zhang, Y. Liu, A. Elzatahry, R. Wang, Y. Xia, D. Al-Dhayan, N. Zheng and D. Zhao, *J. Am. Chem. Soc.*, 2018, **140**, 4135–4143.
256 H. Liu, Z. Bi, X.-G. Sun, R. R. Unocic, M. P. Paranthaman, S. Dai and G. M. Brown, *Adv. Mater.*, 2011, **23**, 3450–3454.
257 W. Li, Z. Wu, J. Wang, A. A. Elzatahry and D. Zhao, *Chem. Mater.*, 2014, **26**, 287–298.
258 W. Li, F. Wang, Y. Liu, J. Wang, J. Yang, L. Zhang, A. A. Elzatahry, D. Al-Dahyan, Y. Xia and D. Zhao, *Nano Lett.*, 2015, **15**, 2186–2193.
259 J. Lee, S. Kim, J.-H. Park, C. Jo, J. Chun, Y.-E. Sung, E. Lim and J. Lee, *J. Mater. Chem. A*, 2020, **8**, 3119–3127.
260 J.-H. Kwon, K. N. Chaudhari, E. Coy, J. H. Seo, S. J. Ahn, Y.-H. Lee, S. Lee, Y. C. Cho, O. Choi, K. S. Lee, D. I. Son and Y. Kim, *ACS Sustain. Chem. Eng.*, 2021, **9**, 16627–16636.
261 Y. Zhao, X. Li, B. Yan, D. Xiong, D. Li, S. Lawes and X. Sun, *Adv. Energy Mater.*, 2016, **6**, 1502175.
262 B. Guo, X. Yu, X.-G. Sun, M. Chi, Z.-A. Qiao, J. Liu, Y.-S. Hu, X.-Q. Yang, J. B. Goodenough and S. Dai, *Energy Environ. Sci.*, 2014, **7**, 2220–2226.

263 J. B. Cook, H.-S. Kim, Y. Yan, J. S. Ko, S. Robbennolt, B. Dunn and S. H. Tolbert, *Adv. Energy Mater.*, 2016, **6**, 1501937.
264 R. R. Salunkhe, Y. V. Kaneti, J. Kim, J. H. Kim and Y. Yamauchi, *Acc. Chem. Res.*, 2016, **49**, 2796–2806.
265 M. S. Kim, E. Lim, S. Kim, C. Jo, J. Chun and J. Lee, *Adv. Funct. Mater.*, 2017, **27**, 1603921.
266 L. Kuang, F. Ji, X. Pan, D. Wang, X. Chen, D. Jiang, Y. Zhang and B. Ding, *Chem. Eng. J.*, 2017, **315**, 491–499.
267 A. G. Pandolfo and A. F. Hollenkamp, *J. Power Sources*, 2006, **157**, 11–27.
268 K. Jost, G. Dion and Y. Gogotsi, *J. Mater. Chem. A*, 2014, **2**, 10776–10787.
269 R. R. Salunkhe, Y. V. Kaneti and Y. Yamauchi, *ACS Nano*, 2017, **11**, 5293–5308.
270 J. Du, Y. Zhang, H. Wu, S. Hou and A. Chen, *Carbon*, 2020, **156**, 523–528.
271 M. Xie, H. Meng, J. Chen, Y. Zhang, C. Du, L. Wan and Y. Chen, *ACS Appl. Energy Mater.*, 2021, **4**, 1840–1850.
272 X. Feng, Y. Bai, M. Liu, Y. Li, H. Yang, X. Wang and C. Wu, *Energy Environ. Sci.*, 2021, **14**, 2036–2089.
273 K. Jayaramulu, S. Mukherjee, D. M. Morales, D. P. Dubal, A. K. Nanjundan, A. Schneemann, J. Masa, S. Kment, W. Schuhmann, M. Otyepka, R. Zbořil and R. A. Fischer, *Chem. Rev.*, 2022, **122**, 17241–17338.
274 L.-N. Han, X. Wei, Q.-C. Zhu, S.-M. Xu, K.-X. Wang and J.-S. Chen, *J. Mater. Chem. A*, 2016, **4**, 16698–16705.
275 H. Peng, B. Yao, X. Wei, T. Liu, T. Kou, P. Xiao, Y. Zhang and Y. Li, *Adv. Energy Mater.*, 2019, **9**, 1803665.
276 J. Zhou, J. Lian, L. Hou, J. Zhang, H. Gou, M. Xia, Y. Zhao, T. A. Strobel, L. Tao and F. Gao, *Nat. Commun.*, 2015, **6**, 8503.
277 X.-H. Li and M. Antonietti, *Angew. Chem., Int. Ed.*, 2013, **52**, 4572–4576.
278 T.-N. Ye, L.-B. Lv, X.-H. Li, M. Xu and J.-S. Chen, *Angew. Chem., Int. Ed.*, 2014, **53**, 6905–6909.
279 X. Xie, C. Hou, D. Wu, X. Sun, X. Yang, Y. Zhang, R. Yu, S. Zhang, H. Kimura and W. Du, *J. Alloys Compd.*, 2022, **891**, 161967.
280 J. Liu, J. Jiang, M. Bosman and H. J. Fan, *J. Mater. Chem.*, 2012, **22**, 2419–2426.
281 H. J. Lee, J. H. Lee, S.-Y. Chung and J. W. Choi, *Angew. Chem., Int. Ed.*, 2016, **55**, 3958–3962.
282 M. Khot and A. Kiani, *Int. J. Energy Res.*, 2022, **46**, 21757–21796.
283 Y. Wang, J. Guo, T. Wang, J. Shao, D. Wang and Y.-W. Yang, *Nanomaterials*, 2015, **5**, 1667–1689.
284 E. Lim, J. Chun, C. Jo and J. Hwang, *Korean J. Chem. Eng.*, 2021, **38**, 227–247.